

Structure-based RNA Design by Step-wise Optimization of Latent Diffusion Model

Qi Si^{1*}, Xuyang Liu^{1*}, Pinglei Wang^{2*}, Xin Guo^{1†}, Yuan Qi^{1,3,4}, Yuan Cheng^{1,3†}

¹Shanghai Academy of Artificial Intelligence for Science

²School of Biomedical Engineering, Shanghai Jiao Tong University

³Artificial Intelligence Innovation and Incubation Institute, Fudan University

⁴Zhongshan Hospital, Fudan University

sqwd0616@gmail.com, wangpinglei@sjtu.edu.cn

Abstract

RNA inverse folding, designing sequences to form specific 3D structures, is critical for therapeutics, gene regulation, and synthetic biology. Current methods, focused on sequence recovery, struggle to address structural objectives like secondary structure consistency (SS), minimum free energy (MFE), and local distance difference test (LDDT), leading to suboptimal structural accuracy. To tackle this, we propose a reinforcement learning (RL) framework integrated with a latent diffusion model (LDM). Drawing inspiration from the success of diffusion models in RNA inverse folding, which adeptly model complex sequence-structure interactions, we develop an LDM incorporating pre-trained RNA-FM embeddings from a large-scale RNA model. These embeddings capture co-evolutionary patterns, markedly improving sequence recovery accuracy. However, existing approaches, including diffusion-based methods, cannot effectively handle non-differentiable structural objectives. By contrast, RL excels in this task by using policy-driven reward optimization to navigate complex, non-gradient-based objectives, offering a significant advantage over traditional methods. In summary, we propose the Step-wise Optimization of Latent Diffusion Model (SOLD), a novel RL framework that optimizes single-step noise without sampling the full diffusion trajectory, achieving efficient refinement of multiple structural objectives. Experimental results demonstrate SOLD surpasses its LDM baseline and state-of-the-art methods across all metrics, establishing a robust framework for RNA inverse folding with profound implications for biotechnological and therapeutic applications.

Code — <https://github.com/darkflash03/SOLD>

Introduction

The RNA inverse folding task involves designing RNA sequences that fold into specific 3D structures, holds significant potential for applications in RNA therapeutics, gene regulation, and synthetic biology (Damase et al. 2021). For instance, rationally designed riboswitches can enable precise control of mRNA translation, paving the way for

targeted therapies (Mustafina, Fukunaga, and Yokobayashi 2019).

Existing RNA inverse folding methods primarily include physics-based and deep learning-based methods. Physics-based approaches like Rosetta (Leman et al. 2020) generate sequences via Monte Carlo optimization but are computationally expensive and struggle with polymorphic conformations. Algorithms based on 2D structures, such as ViennaRNA (Churkin et al. 2018), achieve computational efficiency but neglect critical 3D geometric information, which restricts their overall applicability. In recent years, deep learning-based methods have gained traction, with generative models showing promise. Unlike variational autoencoders, as RhoDesign (Wong et al. 2024) and RDesign (Tan et al. 2024), which struggle with complex distributions and long-range dependencies, diffusion models excel at capturing intricate sequence-structure interactions through iterative denoising. RiboDiffusion (Huang et al. 2024a) proposed a diffusion-based framework for RNA inverse folding, but it depends on direct sequence modeling, which may not fully capture the rich co-evolutionary context inherent in RNA sequences.

RL has recently been widely applied to optimize the generation objectives of diffusion models. For instance, DDPO (Black et al. 2023) and DPOK (Fan et al. 2023) combined diffusion models with policy optimization to optimize decision-making in continuous action spaces. These studies demonstrate that RL can guide diffusion models to optimize objectives that are difficult to address directly with traditional methods by designing specific reward functions. Therefore, RL is particularly well-suited for diffusion models in RNA inverse folding, as it effectively optimizes non-differentiable structural metrics. Despite its potential, RL remains underexplored in this area.

To address the above limitations, we propose SOLD, a LDM based framework for RNA inverse folding. SOLD leverages the embedding space of the RNA-FM (Chen et al. 2022) to capture co-evolutionary information. Furthermore, SOLD introduces a novel step-wise RL optimization strategy that directly optimizes structural metrics (SS, MFE, LDDT), where step-wise refers to starting from any noise time step and independently optimizing each reverse sampling step. This approach ensures both computational ef-

*These authors contributed equally.

†Corresponding author.

Copyright © 2026, Association for the Advancement of Artificial Intelligence (www.aaai.org). All rights reserved.

iciency and superior performance in generating RNA sequences that align with target structures. Our main contributions are as follows:

- A LDM that leverages pre-trained LLM embedding to improve sequence recovery in RNA design.
- The first integration of RL into LDM for RNA inverse folding, enabling effective optimization of complex structural objectives.
- A step-wise RL optimization algorithm that achieves faster convergence and superior performance.

Related Work

RNA Inverse Folding Methods

RNA inverse folding designs sequences for specified structures, categorized into physics-based, heuristic, and deep learning approaches. Physics-based Rosetta (Das, Karanicolas, and Baker 2010; Leman et al. 2020) uses Monte Carlo sampling with energy functions but is computationally intensive. Early 2D structure-based approaches such as RNAinverse (Hofacker et al. 1994) and ViennaRNA (Lorenz et al. 2011) were dynamically programmed directly on Rfam (Griffiths-Jones et al. 2003), thus ignoring 3D structural information. Among the heuristics, INFO-RNA (Busch et al. 2006) performs a direct random search of the structure, whereas methods such as RNASSD (Andronescu et al. 2004), antaRNA (Kleinkauf, Mann, and Backofen 2015), aRNAQ (Merleau and Smerlak 2022), eM2dRNAs (Álvaro Rubio-Largo et al. 2023), and MCTS-RNA (Yang, Yoshizoe, and Tsuda 2017) use global search or evolutionary approaches.

Deep learning methods such as gRNADe (Joshi et al. 2025) is a concurrent graph-based RNA refolding method, while RhoDesign (Wong et al. 2024), RDesign (Tan et al. 2024), PiFold (Gao, Tan, and Li 2023), StructGNN (Chou et al. 2024), and GVP-GNN (Jing et al. 2021) are representative deep learning methods for inverse folding, which are modified here for RNA compatibility. Recently, RISoTTo (Bibekar, Krapp, and Dal Peraro 2025) proposed a context-aware geometric deep learning framework that integrates structural context into RNA sequence design. While these deep learning approaches enhance the quality of generated sequences, they are unable to directly optimize structure metrics, such as MFE and LDDT.

Diffusion Models in Molecular Generation

RiboDiffusion (Huang et al. 2024a) applies 3D diffusion on PDB dataset for RNA inverse folding. DRAKES (Wang et al. 2024) fine-tunes discrete diffusion with reinforcement learning, optimizing DNA enhancer activity and protein stability. GradeIF (Yi et al. 2023) leverages graph denoising with BLOSUM matrices, enhancing protein sequence diversity and recovery. RNAdiffusion (Huang et al. 2024b) uses latent diffusion to generate RNA sequences, optimizing the translation efficiency. Structured DDPM (Austin et al. 2021) and Dirichlet Flow (Stark et al. 2024) explored discrete diffusion on molecular data. RNAFlow (Chen et al. 2024) integrates 2D/3D diffusion in RNA structures. These models

address diverse molecular design challenges, from structure prediction to functional optimization.

Reinforcement Learning for Generative Model Optimization

RL has emerged as a powerful approach for optimizing generative models, particularly diffusion models, by aligning them with diverse objectives. Online RL methods like PPO (Schulman et al. 2017) and RAFT (Dong et al. 2023) leverage direct reward optimization, while offline methods such as DPO (Rafailov et al. 2023) utilize preference datasets for policy alignment.

Meanwhile, alignment of diffusion models to preferences by reinforcement learning has also been widely explored. DDPO (Black et al. 2023) and DPOK (Fan et al. 2023) use the PPO algorithm to enhance image quality in diffusion models; Diffusion-DPO (Wallace et al. 2023) adapts DPO to fine-tune Stable Diffusion XL with human preferences. These studies demonstrate the ability of RL to guide models toward optimizing objectives that traditional methods struggle to address directly.

Comparison with Our Work

SOLD integrates latent diffusion and RL to advance RNA inverse folding, offering some significant advantages over existing methods:

- Unlike RNAdiffusion, which generates sequences without structural constraints and optimizes functional metrics using separately trained reward models, SOLD focuses on structure-based RNA design, directly optimizing structural metrics. By leveraging ViennaRNA for direct evaluation, SOLD eliminates the need for additional reward models, reducing computational overhead and mitigating inaccuracies from reward model predictions.
- DRAKES utilizes discrete diffusion with RL to optimize a single objective for RNA design, relying on differentiable reward models that introduce additional training costs and the potential risk of over-optimization. However, SOLD operates in a continuous latent space for diffusion, enabling efficient optimization of multiple RNA-specific metrics without the need for separately trained reward models.
- In contrast to DDPO and DPOK, which are designed for image and text generation and rely on sampling complete trajectories, incurring high computational costs, SOLD is tailored for RNA inverse folding, and its step-wise RL optimization iteratively refines strategies, achieving greater efficiency compared to trajectory-based methods.

Methods

Latent Diffusion Model

The SOLD employs a latent diffusion model (LDM) to generate RNA sequences, integrating pre-trained RNA-FM to extract embeddings with geometric information from the backbone, producing sequences that conform to specific structural and functional properties as Figure 1. We map RNA sequences directly into variable-length embeddings of

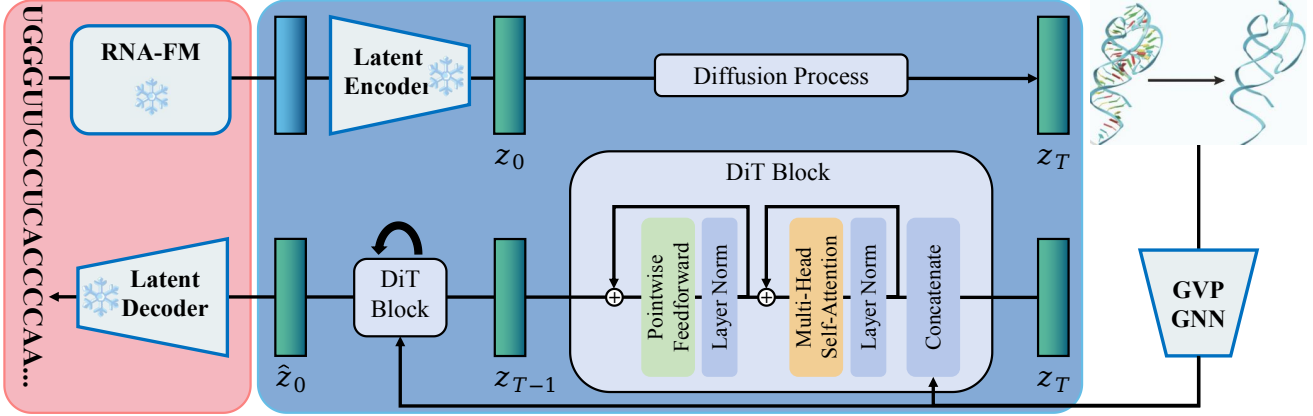


Figure 1: The LDM encodes RNA-FM embeddings into a latent representation, performs denoising with GVP-GNN + DiT blocks, and decodes the refined latent into RNA sequences consistent with structural constraints.

shape $(L, 640)$, where L represents the sequence length. These embeddings are compressed into a latent representation of shape (L, D) via an MLP encoder to improve the efficiency of the diffusion process.

A denoising network π_θ , integrated with GVP-GNN (Jing et al. 2021) and Diffusion Transformer (DiT) (Peebles and Xie 2023), is used to predict the denoised latent embedding \hat{z}_0 at time $t = 0$. The MLP decoder reconstructs the latent embedding \hat{z}_0 into a sequence probability distribution $(L, 4)$, generating sequences of length L that align with the input backbone structure.

The forward process of diffusion introduces Gaussian noise to the latent embedding $z_0 \in \mathbf{R}^{L \times D}$:

$$q(z_t | z_{t-1}) = \mathcal{N}(z_t; \sqrt{1 - \beta_t} z_{t-1}, \beta_t I) \quad (1)$$

where β_t is the noise schedule, and $t = 1, \dots, T$. The reverse process reconstructs the embedding by predicting $\hat{z}_0 = \pi_\theta(z_t, t, c)$:

$$p_\theta(z_{t-1} | z_t, c) = \mathcal{N}(z_{t-1}; \mu_\theta(z_t, t, c), \sigma_t^2 I) \quad (2)$$

with the mean defined as:

$$\mu_\theta(z_t, t, c) = \frac{\sqrt{\alpha_t}(1 - \bar{\alpha}_{t-1})}{1 - \bar{\alpha}_t} z_t + \frac{\sqrt{\bar{\alpha}_{t-1}}(1 - \alpha_t)}{1 - \bar{\alpha}_t} \hat{z}_0 \quad (3)$$

where c represents the geometric information from backbone, $\alpha_t = 1 - \beta_t$, $\bar{\alpha}_t = \prod_{i=1}^t \alpha_i$, and the variance is defined as $\sigma_t^2 = \frac{(1 - \bar{\alpha}_{t-1})(1 - \alpha_t)}{1 - \bar{\alpha}_t}$.

The training objective combines MSE and cross-entropy:

$$\mathcal{L} = \mathbb{E}_{z_0, t} [\|z_0 - \hat{z}_0\|^2] - \mathbb{E}_s \left[\sum_{i=1}^L \log p(s_i | \text{Dec}(\hat{z}_0)_i) \right] \quad (4)$$

The first term of the loss function, denoted as the mean squared error (MSE) term, quantifies the difference between the true latent embedding z_0 and the single-step predicted embedding \hat{z}_0 , enhancing the precision of denoising network in predicting the clean embedding. The second term referred

to the cross-entropy term, ensures that the sequence decoded from the final denoised embedding \hat{z}_0 closely aligns with the target sequence s , guiding the frozen decoder to generate accurate nucleotide probability distributions.

The encoder efficiently compresses RNA-FM embeddings into the latent space, thereby facilitating the diffusion process.

$$z_0 = \text{Enc}_\psi(h) = \text{MLP}_\psi(h) \quad (5)$$

where $h \in \mathbf{R}^{L \times 640}$ represents the input embedding, and $z_0 \in \mathbf{R}^{L \times D}$ is the compressed latent representation. The decoder generates sequence probabilities by:

$$p(s) = \text{Dec}_\phi(\hat{z}_0) = \text{softmax}(\text{MLP}_\phi(\hat{z}_0)) \quad (6)$$

where $\hat{z}_0 \in \mathbf{R}^{L \times D}$ is the final denoised latent embedding, and $p(s) \in \mathbf{R}^{L \times 4}$ represents the probability distribution over the four nucleotide bases (A, U, C, G).

Step-wise Optimization of Latent Diffusion Model

The SOLD algorithm refines the pre-trained LDM through a RL framework, targeting complex objectives critical for RNA inverse folding, such as SS, MFE, and LDDT. The overall architecture is depicted in Figure 2. SOLD adopts a single-step sampling strategy inspired by Denoising Diffusion Implicit Models (DDIM) (Song, Meng, and Ermon 2020) to enhance computational efficiency. In DDIM, the reverse process is approximated with a deterministic mapping, enabling single-step predictions of the target latent embedding \hat{z}_0 from a noisy sample z_t .

SOLD’s single-step prediction leverages the Denoising Diffusion Implicit Model (DDIM) framework to efficiently generate denoised latent embeddings. The sampling process is defined as:

$$z'_{t-k} = \sqrt{\bar{\alpha}_{t-k}} \hat{z}_0 + \gamma_{t-k} \epsilon_\theta(z_t, t, c) + \sigma_{t-k} \epsilon \quad (7)$$

where $\hat{z}_0 = \pi_\theta(z_t, t, c)$ is the predicted target embedding at $t = 0$, $\gamma_{t-k} = \sqrt{1 - \bar{\alpha}_{t-k} - \sigma_{t-k}^2}$ is a shorthand coefficient, $\epsilon_\theta(z_t, t, c) = \frac{z_t - \hat{z}_0 \sqrt{\bar{\alpha}_t}}{\sqrt{1 - \bar{\alpha}_t}}$ is the predicted noise conditioned on structural constraints c , and $\epsilon \sim \mathcal{N}(0, I)$ is

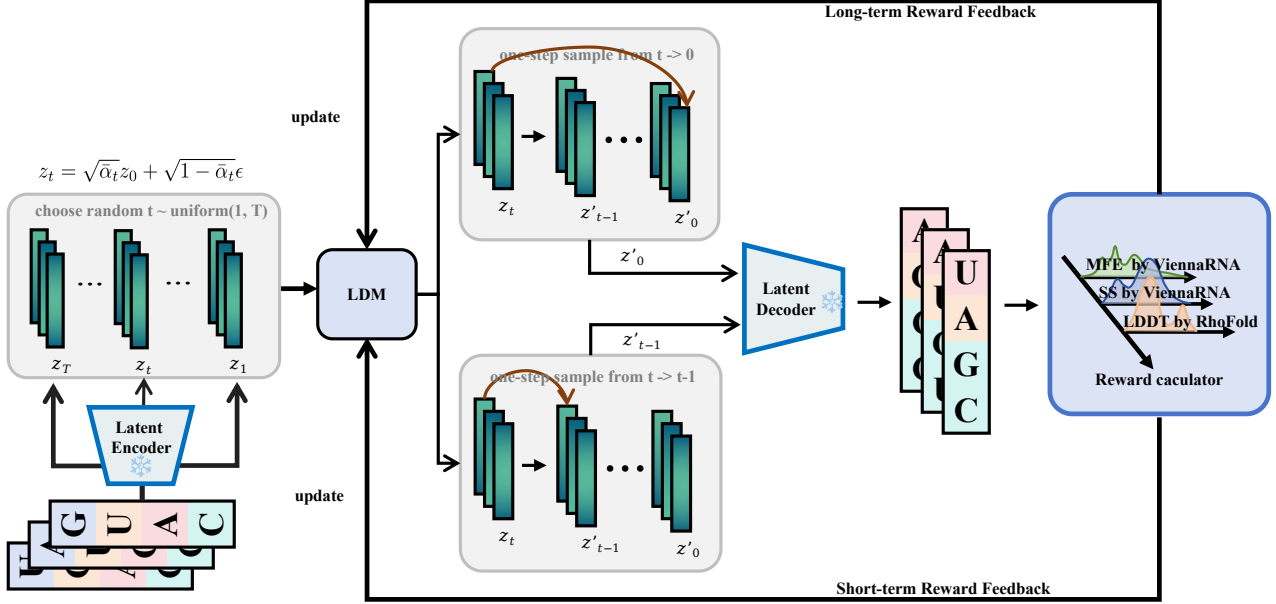


Figure 2: An overview of the SOLD. SOLD utilizes long-term and short-term reward feedback to directly optimize trained latent denoising model in a random denoising step.

standard Gaussian noise. The stochasticity is controlled by $\sigma_{t-k}^2 = \eta \cdot \frac{(1-\bar{\alpha}_{t-k})(1-\alpha_t)}{1-\bar{\alpha}_t}$, with hyperparameter η . When $k = t$, SOLD can sample z'_0 in a single step, significantly enhancing computational efficiency. By decoding z'_0 into a sequence s'_0 , SOLD evaluates a long-term reward $r_0(t) = R_i(s'_0)$, where R_i assesses RNA-specific objectives.

By randomly sampling a timestep t and directly predicting z'_0 from z_t , SOLD eliminates the need to generate complete trajectories during training, reducing computational complexity. Notably, while SOLD uses single-step sampling for training efficiency, it retains full trajectory denoising during inference to ensure high-quality sequence generation.

In early denoising steps (large t), the smaller $\bar{\alpha}_t$ increases the variance of the noise term, reducing the accuracy of direct z'_0 predictions and the reliability of long-term rewards $r_0(t)$. To address this, SOLD computes short-term rewards by equation 7 with sampling strategy ($k = 1$) to predict the intermediate latent embedding z'_{t-1} from z_t . By decoding z'_{t-1} into a sequence s'_{t-1} , SOLD computes a short-term reward $r_t(t) = R_i(s'_{t-1})$, using the same reward function R_i as the long-term reward. This short-term rewards effectively guide learning during early denoising steps where high noise levels diminish the reliability of long-term rewards.

To balance the strengths of both rewards, SOLD integrates long-term and short-term rewards through a piecewise reward function:

$$r_{\text{total}}(t) = w(t) \cdot r_t(t) + u(t) \cdot r_0(t) \quad (8)$$

where $w(t)$ and $u(t)$ are time-dependent weighting functions. In early denoising steps (large t), $w(t) = 1$ and $u(t) = 0$, prioritizing the short-term reward $r_t(t)$ to guide learning. In later denoising steps (small t), $w(t) = 0$ and $u(t) = 1$,

emphasizing the long-term reward $r_0(t)$. This piecewise strategy enhances SOLD’s flexibility in optimizing RNA-specific objectives across different denoising stages.

SOLD optimizes the model parameters θ using Proximal Policy Optimization (PPO) (Schulman et al. 2017) based on the total reward $r_{\text{total}}(t)$, with the objective:

$$\mathcal{J}_{\text{SOLD}}(\theta) = \mathbb{E}_{t \sim \mathcal{U}[1, T], c, z_t, z'_0 \sim p_{\theta}(z'_0 | z_t, c)} [r_{\text{total}}(t)] \quad (9)$$

where the policy gradient is computed via the REINFORCE algorithm with importance sampling:

$$\nabla_{\theta} \mathcal{J}_{\text{SOLD}} = \mathbb{E}_{p_{\text{old}}(t)} [w \nabla_{\theta} \log p_{\theta}(z'_0 | z_t, t, c) r(z_t)] \quad (10)$$

where the importance weight is:

$$w = \frac{p_{\theta}(z'_0 | x_t, t, c)}{p_{\text{ref}}(z'_0 | x_t, t, c)} \quad (11)$$

with $p_{\text{ref}}(z'_0 | z_t, t, c)$ representing the conditional probability, under the previous iteration’s model parameters θ_{ref} .

SOLD adopts a clipped surrogate objective, with a clip range of $\epsilon = 0.0001$, to ensure stable policy updates. Additionally, SOLD incorporates a constraint to limit divergence between the current policy p_{θ} and the previous policy p_{ref} :

$$\mathcal{J}_{\text{ref}}(\theta) = -D_{\text{KL}}(p_{\theta} \| p_{\text{ref}}) \quad (12)$$

Finally, the total optimization objective is:

$$\mathcal{J}_{\text{SOLD}}^{\text{reg}}(\theta) = \mathcal{J}_{\text{SOLD}}(\theta) + \lambda_{\text{ref}} \mathcal{J}_{\text{ref}}(\theta) \quad (13)$$

where λ_{ref} is the regularization weight for the reference policy. This integration of single-step sampling, piecewise reward framework, and KL-constrained optimization enables SOLD to effectively tackle complex RNA inverse folding design.

Method	SOLD TEST		CASP15 TEST	
	Sequence Recovery	NT Recovery	Sequence Recovery	NT Recovery
RhoDesign	0.2734	0.2859	0.2606	0.2575
RDesign	0.4457	0.3966	0.3264	0.3251
gRNAd	0.5108	0.4890	0.5097	0.5149
RiboDiffusion	0.5125	0.4416	0.5388	0.3871
DRAKES-Pretrain	0.4524	0.4088	0.3357	0.3374
LDM	0.5728	0.5034	0.5462	0.5473

Table 1: Sequence Recovery and NT Recovery Comparison

Experiment

To evaluate the performance of SOLD for RNA inverse folding, we conducted a series of experiments. Our experiments leverage a high-quality dataset constructed from the RCSB Protein Data Bank, RNAsolo, and CASP15 RNA dataset, as detailed in Appendix A. The dataset was pre-processed by clustering RNA structural data using PSI-CD-HIT (sequence threshold: 0.3) and US-align (structural threshold: 0.45). After pre-processing, we obtained 8222 structures, split into pre-training (7067 structures), RL fine-tuning (389 structures), and SOLD TEST (766 structures) datasets, with deduplication to prevent information leakage. The CASP15 TEST dataset served as an independent test benchmark.

We compared SOLD against state-of-the-art (SOTA) methods, including RhoDesign (Wong et al. 2024), RDesign (Tan et al. 2024), gRNAd (Joshi et al. 2025), RiboDiffusion (Huang et al. 2024a), and DRAKES (Wang et al. 2024). Notably, DRAKES-Pretrain refers to the pre-trained DRAKES model without RL finetuning, while DRAKES incorporates optimization for a single metric (MFE), using a discrete diffusion framework with differentiable reward models. In contrast, SOLD employs LDM with step-wise RL optimization, targeting multiple structurally relevant metrics without any differentiable reward model.

The experiments are structured in three parts: (1) evaluating the LDM’s superiority in 1D metrics (Sequence Recovery, Nucleotide (NT) Recovery) to test its foundational generative capability; (2) assessing SOLD’s RL finetuning for single-objective optimization, evaluating its speed and effectiveness in optimizing 2D (SS, MFE) and 3D (LDDT) metrics; and (3) validating the effectiveness of SOLD’s weighted multi-objective optimization across 1D (Sequence Recovery), 2D (SS, MFE), and 3D (RMSD, LDDT) metrics, with a practical case study to examine SOLD’s real-world utility in RNA design. All experiments were conducted on a single A100 GPU.

LDM Performance on Sequence Generation

To assess the effectiveness of the LDM backbone in SOLD, we evaluated its sequence generation performance using 1D metrics, specifically Sequence Recovery and NT Recovery, which measure the similarity of generated sequences to target sequences and the accuracy of nucleotide composition, respectively. These metrics focus on the model’s ability to predict the correct nucleotide at each position, with structural information serving as input features that implicitly

influence sequence generation rather than as explicit optimization targets. As the pre-training phase of LDM focuses on optimizing sequence prediction rather than directly targeting 2D or 3D structural metrics, we evaluate performance only using 1D metrics. Table 1 presents the results on the SOLD TEST and CASP15 TEST datasets, comparing SOLD’s LDM against RhoDesign, RDesign, gRNAd, RiboDiffusion, and DRAKES-Pretrain. Since this evaluation precedes RL finetuning, we compare against DRAKES-Pretrain to ensure a fair assessment of pre-trained models. LDM consistently outperforms competitors, showing higher Sequence Recovery and NT Recovery across both test datasets. Compared with RiboDiffusion, which performs SDE-based diffusion directly in the one-hot RNA sequence space, our LDM operates in the RNA-FM embedding space while keeping the backbone architecture unchanged. This latent representation captures richer structural and co-evolutionary features, leading to markedly improved sequence recovery. This method appears to enhance sequence prediction accuracy while maintaining computational efficiency, establishing a strong foundation for subsequent RL finetuning.

RL Finetuning for Single-Objective Optimization

We evaluated SOLD’s RL finetuning stage for single-objective optimization, targeting on 2D (SS, MFE) and 3D (LDDT) metrics, which are critical for RNA functionality but challenging to optimize directly in SOTA RNA design algorithms. Table 2 presents the results of single-objective optimization for MFE, SS, and LDDT on the SOLD TEST and CASP15 TEST datasets, comparing SOLD against its LDM baseline, DDPO, and DPOK. For MFE optimization, we additionally compared the DRAKES-Pretrain and DRAKES methods to elucidate the impact of reinforcement learning. As DRAKES exclusively optimizes MFE, it was not included in comparisons for SS and LDDT.

For MFE, SOLD demonstrates a better improvement over its LDM baseline compared to the improvement of DRAKES over DRAKES-Pretrain, while also achieving superior final performance. Across all objectives (MFE, SS, LDDT), SOLD consistently improves upon LDM, with varying degrees of enhancement depending on the metric. Figure 3 illustrates the rapid convergence of SOLD compared to DDPO and DPOK, highlighting its efficiency in optimizing these structurally relevant metrics. Table 3 further quantifies this efficiency, revealing that SOLD completes a single training round for each objective much faster than

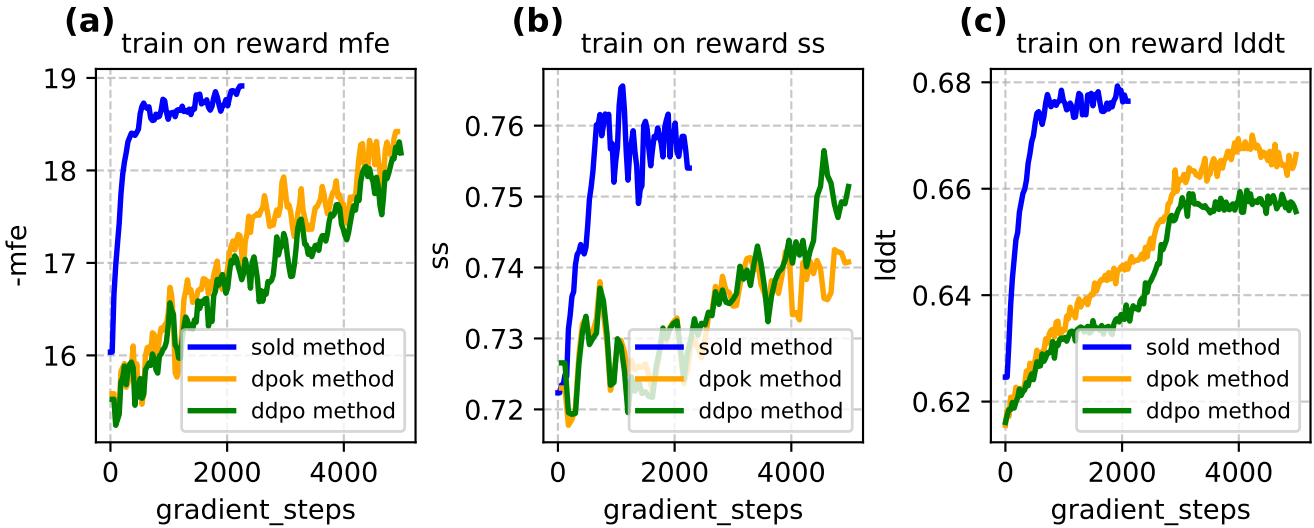


Figure 3: rewards for SOLD, DPOK, and DDPO with MFE, SS, and LDDT as reward objectives: (a) MFE, (b) SS, (c) LDDT.

Method	SOLD TEST	CASP15 TEST
MFE Training (MFE reward) ↓		
DRAKES-Pretrain	-12.5123	-52.6827
DRAKES	-14.2374	-61.0354
LDM	-13.1519	-52.7387
DDPO	-18.7498	-63.9567
DPOK	-17.4660	-67.7949
SOLD	-19.7428	-68.2100
SS Training (SS reward) ↑		
LDM	0.7274	0.5543
DDPO	0.7595	0.6649
DPOK	0.7511	0.6303
SOLD	0.7551	0.7010
LDDT Training (LDDT reward) ↑		
LDM	0.6184	0.3237
DDPO	0.6286	0.3406
DPOK	0.6329	0.3351
SOLD	0.6384	0.3548

Table 2: Single-Objective Reward Comparison

DDPO and DPOK. For LDDT, SOLD’s training speed is slightly slower due to the computational bottleneck of structure prediction, but it still remains competitive. Table 2 further confirms that the performance of SOLD on MFE, SS, and LDDT is generally on par with or superior to DDPO and DPOK, demonstrating its effectiveness alongside its speed advantage.

SOLD’s step-wise RL optimization, utilizing single-step sampling, accelerates convergence compared to trajectory-based methods like DDPO and DPOK. Additionally, the integration of ViennaRNA for direct reward evaluation eliminates the need for separate reward models, enhancing both efficiency and effectiveness in optimizing these challenging metrics.

Method	MFE (s)	SS (s)	LDDT (s)
DDPO	5953	6190	14000
DPOK	7677	7330	14200
SOLD	256	263	6900

Table 3: Average training time per epoch for DDPO, DPOK, and SOLD across different objectives

Multi-Objective Optimization Performance

To validate SOLD’s capability for weighted multi-objective optimization, we conducted experiments targeting the simultaneous improvement of 1D, 2D, and 3D metrics. To ensure generality, we applied this weighting without tuning hyperparameters. We optimize SS, MFE, and LDDT using an equal weighting scheme, addressing the differing scales by mapping MFE to the (0,1) interval with the function:

$$\text{reward}_{\text{MFE}} = \exp\left(\frac{1}{\text{MFE} - \frac{1}{4}}\right) \quad (14)$$

Table 4 compares SOLD against SOTA RNA design methods on the SOLD TEST and CASP15 TEST datasets. SOLD consistently outperforms existing methods across nearly all metrics, demonstrating a superior balance between sequence naturalness and structural fidelity. Compared to its LDM baseline, SOLD maintains or improves sequence recovery with notable improvements in SS, MFE, LDDT, and RMSD. This balanced enhancement underscores SOLD’s ability to optimize multiple objectives without sacrificing any single metric. The practical efficacy of SOLD is further demonstrated with a TPP-specific riboswitch case study (Figure 4). Here, SOLD successfully designed a sequence that folds into the precise target structure, whereas other methods failed, producing conformations distant from the goal. This case confirms SOLD’s capacity to satisfy stringent structural and functional constraints.

SOLD TEST					
Method	Sequence Recovery \uparrow	MFE \downarrow	SS \uparrow	RMSD \downarrow	LDdT \uparrow
RhoDesign	0.2734	-11.9212	0.6499	16.3577	0.5031
RDesign	0.4457	-10.6990	0.6135	16.1315	0.5238
gRNAd	0.5108	-10.5409	0.5624	17.9960	0.4848
RiboDiffusion	0.5125	-15.2128	0.7632	12.3170	0.6102
DRAKES	0.4400	-14.2374	0.7691	11.9077	0.6191
LDM	0.5728	-13.3275	0.7269	12.5732	0.6178
SOLD	0.5732	-16.8611	0.7601	11.8612	0.6360
CASP15 TEST					
Method	Sequence Recovery \uparrow	MFE \downarrow	SS \uparrow	RMSD \downarrow	LDdT \uparrow
RhoDesign	0.2606	-45.9620	0.4708	30.2765	0.3306
RDesign	0.3264	-37.0679	0.4239	30.0221	0.3165
gRNAd	0.5097	-40.8491	0.4186	30.8809	0.3121
RiboDiffusion	0.5388	-41.1593	0.4699	29.5904	0.3210
DRAKES	0.3484	-61.0354	0.6412	27.1322	0.3587
LDM	0.5462	-52.7387	0.5543	29.7038	0.3237
SOLD	0.5888	-64.0375	0.6957	26.8422	0.3680

Table 4: Multi-Objective Performance Comparison

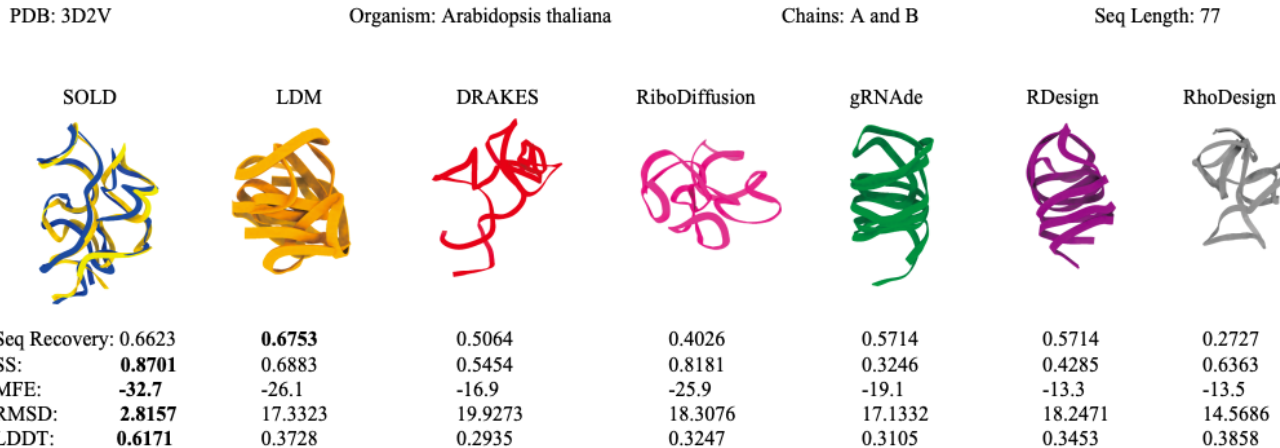


Figure 4: Comparison of rna design methods for example (PDB: 3D2V), ground-truth structure (gold), SOLD (blue)

Conclusion

In this paper, we introduce SOLD, a novel RNA inverse folding framework that integrates a latent diffusion model (LDM) with reinforcement learning (RL) for superior performance. Combining RNA-FM embeddings with 3D backbone geometric features, SOLD’s LDM excels in sequence recovery, laying a strong foundation for sequence generation. A step-wise RL algorithm further enhances performance over the LDM baseline, optimizing structurally relevant metrics with improved convergence efficiency compared to RL methods requiring full trajectory sampling. This approach represents a highly competitive algorithm that balances sequence naturalness with structural fidelity, positioning SOLD as a powerful tool for RNA design with potential for applications in therapeutics and biotechnology.

However, SOLD’s performance is constrained by the limited availability of high-quality RNA structural data. Additionally, we have not extensively explored how 1D, 2D, and 3D metrics interact and coordinate in RNA design. More-

over, current reward evaluation tools, such as ViennaRNA and RhoFold, inevitably introduce approximation errors that may affect optimization accuracy. Nonetheless, our proposed framework is modular and tool-agnostic — the reward component is fully pluggable, allowing seamless substitution with more accurate structure prediction or energy evaluation models as they become available. In future work, we aim to expand datasets, refine reward evaluation with improved predictors, and explore synergistic optimization of multi-scale metrics, further enhancing SOLD’s robustness and generalizability for diverse RNA design challenges.

Acknowledgments

This work was supported by the National Natural Science Foundation of China (Grant Nos. 82394432 and 92249302), and the Shanghai Municipal Science and Technology Major Project (Grant No. 2023SHZDZX02). The authors acknowledge support from the AI for Science Program, Shanghai Municipal Commission of Economy and Information.

References

Andronescu, M.; Fejes, A. P.; Hutter, F.; Hoos, H. H.; and Condon, A. 2004. A New Algorithm for RNA Secondary Structure Design. *Journal of Molecular Biology*, 336(3): 607–624.

Austin, J.; Johnson, D. D.; Ho, J.; Tarlow, D.; and van den Berg, R. 2021. Structured Denoising Diffusion Models in Discrete State-Spaces. *arXiv preprint arXiv:2107.03006*.

Berman, H. M.; Westbrook, J.; Feng, Z.; Gilliland, G.; Bhat, T. N.; Weissig, H.; Shindyalov, I. N.; and Bourne, P. E. 2000. The Protein Data Bank. *Nucleic Acids Research*, 28(1): 235–242.

Bibekar, P.; Krapp, L. F.; and Dal Peraro, M. 2025. Context-aware geometric deep learning for RNA sequence design. *bioRxiv*. Preprint.

Black, K.; Janner, M.; Du, Y.; Kostrikov, I.; and Levine, S. 2023. Training diffusion models with reinforcement learning. *arXiv preprint arXiv:2305.13301*.

Busch; Anke; Backofen; and Rolf. 2006. INFO-RNA—a fast approach to inverse RNA folding. *Bioinformatics*, 22(15): 1823–1831.

Chen, C.; Zhang, H.; Feng, X.; Shen, K.; Zhang, Y.; and Li, Y. 2024. RNAFlow: RNA Structure and Sequence Design via Inverse Folding-based Flow Matching. *arXiv preprint arXiv:2405.11009*.

Chen, J.; Hu, Z.; Sun, S.; Tan, Q.; Wang, Y.; Yu, Q.; Zong, L.; Hong, L.; Xiao, J.; Shen, T.; et al. 2022. Interpretable RNA foundation model from unannotated data for highly accurate RNA structure and function predictions. *arXiv preprint arXiv:2204.00300*.

Chou, Y.-T.; Chang, W.-T.; Jean, J. G.; Chang, K.-H.; Huang, Y.-N.; and Chen, C.-S. 2024. StructGNN: An efficient graph neural network framework for static structural analysis. *Computers & Structures*, 299: 107385.

Churkin, A.; Retwitzer, M. D.; Reinhartz, V.; Ponty, Y.; Waldspühl, J.; and Barash, D. 2018. Design of RNAs: Comparing Programs for Inverse RNA Folding. *Briefings in Bioinformatics*, 19(2): 350–358.

Dalla-Torre, H.; Gonzalez, L.; Mendoza-Revilla, J.; Carranza, N. L.; Grzywaczewski, A. H.; Oteri, F.; Dallago, C.; Trop, E.; de Almeida, B. P.; Sirelkhatim, H.; Richard, G.; Skwark, M.; Beguir, K.; and Pierrot, M. L. . T. 2025. Nucleotide Transformer: building and evaluating robust foundation models for human genomics. *Nature Methods*, 22.

Damase, T. R.; Sukhovershin, R.; Boada, C.; Taraballi, F.; Pettigrew, R. I.; and Cooke, J. P. 2021. The Limitless Future of RNA Therapeutics. *Frontiers in Bioengineering and Biotechnology*, 9: 628137.

Das, R.; Karanicolas, J.; and Baker, D. 2010. Atomic accuracy in predicting and designing noncanonical RNA structure. *Nature Methods*, 7(4): 291–294.

Das, R.; Kretsch, R. C.; Simpkin, A. J.; Mulvaney, T.; Pham, P.; Rangan, R.; Bu, F.; Keegan, R. M.; Topf, M.; Rigden, D. J.; Miao, Z.; and Westhof, E. 2023. Assessment of three-dimensional RNA structure prediction in CASP15. *Proteins*, 91(12): 1747–1770.

Dong, H.; Xiong, W.; Goyal, D.; Zhang, Y.; Chow, W.; Pan, R.; Diao, S.; Zhang, J.; Shum, K.; and Zhang, T. 2023. Raft: Reward ranked finetuning for generative foundation model alignment. *arXiv preprint arXiv:2304.06767*.

Fan, Y.; Watkins, O.; Du, Y.; Liu, H.; Ryu, M.; Boutilier, C.; Abbeel, P.; Ghavamzadeh, M.; Lee, K.; and Lee, K. 2023. DPOK: Reinforcement Learning for Fine-tuning Text-to-Image Diffusion Models. *Proceedings of the 37th Conference on Neural Information Processing Systems (NeurIPS 2023)*. ArXiv:2305.16381.

Gao, Z.; Tan, C.; and Li, S. Z. 2023. PiFold: Toward effective and efficient protein inverse folding. In *International Conference on Learning Representations*.

Griffiths-Jones, S.; Bateman, A.; Marshall, M.; Khanna, A.; and Eddy, S. R. 2003. Rfam: an RNA family database. *Nucleic acids research*, 31(1): 439–441.

Ho, J.; Jain, A.; and Abbeel, P. 2020. Denoising Diffusion Probabilistic Models. *arXiv preprint arxiv:2006.11239*.

Hofacker, I. L.; Fontana, W.; Stadler, P. F.; Bonhoeffer, S.; Tacker, M.; and Schuster, P. 1994. Fast Folding and Comparison of RNA Secondary Structures. *Monatshefte für Chemie / Chemical Monthly*, 125(9): 167–188.

Huang, H.; Lin, Z.; He, D.; Hong, L.; and Li, Y. 2024a. RiboDiffusion: Tertiary Structure-based RNA Inverse Folding with Generative Diffusion Models. *Bioinformatics*, 40(Suppl 1): i347–i356. Presented at ISMB 2024.

Huang, K.; Yang, Y.; Fu, K.; Chu, Y.; Cong, L.; and Wang, M. 2024b. Latent Diffusion Models for Controllable RNA Sequence Generation. *arXiv preprint arXiv:2409.09828*.

Jing, B.; Eismann, S.; Suriana, P.; Townshend, R. J. L.; and Dror, R. 2021. Learning from Protein Structure with Geometric Vector Perceptrons. In *International Conference on Learning Representations*.

Joshi, C. K.; Jamasb, A. R.; Viñas, R.; Harris, C.; Mathis, S. V.; Morehead, A.; Anand, R.; and Liò, P. 2025. gRNNAde: Geometric Deep Learning for 3D RNA inverse design. In *International Conference on Learning Representations (ICLR)*.

Jumper, J.; Evans, R.; Pritzel, A.; Green, T.; Figurnov, M.; Ronneberger, O.; Tunyasuvunakool, K.; Bates, R.; Žikelić, A.; Potapenko, A.; Bridgland, A.; Meyer, C.; Kohl, S. A. A.; Ballard, A. J.; Cowie, A.; Romera-Paredes, B.; Nikolov, S.; Jain, R.; Adler, J.; Back, T.; Petersen, S.; Reiman, D.; Clancy, E.; Zielinski, M.; Steinegger, M.; Pacholska, M.; Berghammer, T.; Bodenstein, S.; Silver, D.; Vinyals, O.; Senior, A. W.; Kavukcuoglu, K.; Kohli, P.; and Hassabis, D. 2021. Highly Accurate Protein Structure Prediction with AlphaFold. *Nature*, 596(7873): 583–589.

Kabsch, W. 1976. A Solution for the Best Rotation to Relate Two Sets of Vectors. *Acta Crystallographica Section A*, 32(5): 922–923.

Kleinkauf, R.; Mann, M.; and Backofen, R. 2015. antaRNA: ant colony-based RNA sequence design. *Bioinformatics*, 31(19): 3114–3121.

Leman, J. K.; Weitzner, B. D.; Lewis, S. M.; Adolf-Bryfogle, J.; Alam, N.; Alford, R. F.; Aprahamian, M.;

Baker, D.; Barlow, K. A.; Barth, P.; et al. 2020. Macromolecular modeling and design in Rosetta: recent methods and frameworks. *Nature methods*, 17(7): 665–680.

Li, S.; Moayedpour, S.; Li, R.; Bailey, M.; Riahi, S.; Kogler-Anele, L.; Miladi, M.; Miner, J.; Zheng, D.; Wang, J.; Balasubramani, A.; Tran, K.; Zacharia, M.; Wu, M.; Gu, X.; Clinton, R.; Asquith, C.; Skaleski, J.; Boeglin, L.; Chivukula, S.; Dias, A.; Montoya, F. U.; Agarwal, V.; Bar-Joseph, Z.; and Jager, S. 2023. CodonBERT: Large Language Models for mRNA design and optimization. *bioRxiv*.

Li, W.; and Godzik, A. 2006. Cd-hit: a fast program for clustering and comparing large sets of protein or nucleotide sequences. *Bioinformatics*, 22(13): 1658–1659.

Lorenz, R.; Bernhart, S. H.; zu Siederdissen, C. H.; Tafer, H.; Flamm, C.; and Hofacker, P. F. S. . I. L. 2011. ViennaRNA Package 2.0. *Algorithms for Molecular Biology*, 6(1): 1–14.

Merleau, N. S. C.; and Smerlak, M. 2022. aRNAque: an evolutionary algorithm for inverse pseudoknotted RNA folding inspired by Lévy flights. *BMC Bioinformatics*, 23.

Mustafina, K.; Fukunaga, K.; and Yokobayashi, Y. 2019. Design of mammalian ON-riboswitches based on tandemly fused aptamer and ribozyme. *ACS Synthetic Biology*, 9(1): 19–25.

Nguyen, E.; Poli, M.; Durrant, M. G.; Kang, B.; Katrekar, D.; Li, D. B.; Bartie, L. J.; Thomas, A. W.; King, S. H.; Brix, G.; Sullivan, J.; Ng, M. Y.; Lewis, A.; Lou, A.; Ermon, S.; Baccus, S. A.; Hernandez-Boussard, T.; Ré, C.; Hsu, P. D.; and Hie, B. L. 2024. Sequence modeling and design from molecular to genome scale with Evo. *Science*.

Peebles, W.; and Xie, S. 2023. Scalable diffusion models with transformers. In *Proceedings of the IEEE/CVF international conference on computer vision*, 4195–4205.

Penić, R. J.; Vlašić, T.; Huber, R. G.; Wan, Y.; and Šikić, M. 2024. RiNALMo: General-Purpose RNA Language Models Can Generalize Well on Structure Prediction Tasks. *arXiv preprint arXiv:2403.00043*.

Rafailov, R.; Sharma, A.; Mitchell, E.; Ermon, S.; Manning, C. D.; and Finn, C. 2023. Direct preference optimization: Your language model is secretly a reward model. *arXiv preprint arXiv:2305.18290*.

Schulman, J.; Wolski, F.; Dhariwal, P.; Radford, A.; and Klimov, O. 2017. Proximal Policy Optimization Algorithms. *arXiv preprint arXiv:1707.06347*.

Shen, T.; Hu, Z.; Sun, S.; Liu, D.; Wong, F.; Wang, J.; Chen, J.; Wang, Y.; Hong, L.; Xiao, J.; et al. 2024. Accurate RNA 3D structure prediction using a language model-based deep learning approach. *Nature Methods*, 1–12.

Skwark, M. J.; Hamada, M.; and Tomii, K. 2022. RNA-solo: an RNA secondary structure comparison tool that tolerates isosteric base pairs. *Bioinformatics*, 38(14): 3668–3676.

Song, J.; Meng, C.; and Ermon, S. 2020. Denoising Diffusion Implicit Models. *arXiv:2010.02502*.

Stark, H.; Jing, B.; Wang, C.; Corso, G.; Berger, B.; Barzilay, R.; and Jaakkola, T. 2024. Dirichlet Flow Matching with Applications to DNA Sequence Design. *arXiv preprint arXiv:2402.05841*.

Tan, C.; Zhang, Y.; Gao, Z.; Hu, B.; Li, S.; Liu, Z.; and Li, S. Z. 2024. RDesign: Hierarchical Data-efficient Representation Learning for Tertiary Structure-based RNA Design. In *The Twelfth International Conference on Learning Representations*.

Wallace, B.; Dang, M.; Rafailov, R.; Zhou, L.; Lou, A.; Purushwalkam, S.; Ermon, S.; Xiong, C.; Joty, S.; and Naik, N. 2023. Diffusion Model Alignment Using Direct Preference Optimization. *arXiv preprint arXiv:2311.12908*.

Wang, C.; Uehara, M.; He, Y.; Wang, A.; Biancalani, T.; Lal, A.; Jaakkola, T.; Levine, S.; Wang, H.; and Regev, A. 2024. Fine-Tuning Discrete Diffusion Models via Reward Optimization with Applications to DNA and Protein Design. *arXiv preprint arXiv:2410.13643*.

Wong, F.; He, D.; Krishnan, A.; Hong, L.; Wang, A. Z.; Wang, J.; Hu, Z.; Omori, S.; Li, A.; Rao, J.; et al. 2024. Deep generative design of RNA aptamers using structural predictions. *Nature Computational Science*, 1–11.

Xiao, Y.; Sun, E.; Jin, Y.; and Wang, W. 2024. RNA-GPT: Multimodal Generative System for RNA Structure Prediction. *arXiv preprint arXiv:2411.08900*.

Yang, X.; Yoshizoe, K.; and Tsuda, A. T. . K. 2017. RNA inverse folding using Monte Carlo tree search. *BMC Bioinformatics*, 18.

Yao, J.; Yang, B.; and Wang, X. 2025. Reconstruction vs. generation: Taming optimization dilemma in latent diffusion models. In *Proceedings of the IEEE/CVF Conference on Computer Vision and Pattern Recognition*.

Yi, K.; Zhou, B.; Shen, Y.; Lio, P.; and Wang, Y. G. 2023. Graph Denoising Diffusion for Inverse Protein Folding. In *Thirty-seventh Conference on Neural Information Processing Systems*.

Zhang, C.; Shine, M.; Pyle, A. M.; and Zhang, Y. 2022. US-align: Universal Structure Alignments of Proteins, Nucleic Acids, and Macromolecular Complexes. *Nat Methods*.

Álvaro Rubio-Largo; Lozano-García, N.; Granado-Criado, J. M.; and Vega-Rodríguez, M. A. 2023. Solving the RNA inverse folding problem through target structure decomposition and Multiobjective Evolutionary Computation. *Applied Soft Computing*, 147: 110779.

A. Dataset Details

To support the SOLD in generating RNA sequences with specific structural and functional properties for RNA inverse folding, we constructed a high-quality dataset from the RCSB Protein Data Bank (Berman et al. 2000), RNA-solo (Skwark, Hamada, and Tomii 2022), and CASP15 (Das et al. 2023) databases. The preparation began with clustering RNA structural data from RCSB and RNAsolo on both sequence and structural aspects. Sequence clustering was performed using PSI-CD-HIT (Li and Godzik 2006) with a threshold of 0.3, yielding 2938 initial clusters, while structural clustering used US-align (Zhang et al. 2022) with a threshold of 0.45, producing 1462 clusters. To reserve CASP15 as an external test dataset (named **CASP15 TEST**), we removed CASP15-related cluster IDs from both sequence and structural clustering files, retaining 13,862 structures and 13,424 sequences. Merging the clustering information resulted in 13,166 structures, which were split based on structural clusters into **Pre-training**, **RL Fine-tuning**, and **SOLD TEST** dataset at a 7:1:2 ratio. Sequence clustering information was used to deduplicate the RL Fine-tuning and SOLD TEST datasets against the Pre-training dataset, and the SOLD TEST dataset was further deduplicated using the RL Fine-tuning dataset’s sequence clusters to prevent information leakage, yielding **8731**, **410**, and **813** sequences for the Pre-training, RL Fine-tuning, and SOLD TEST datasets, respectively.

Sequence length distributions were analyzed for the Pre-training, RL Fine-tuning, and SOLD TEST datasets, categorizing sequences as short (≤ 64 nucleotides), medium ($64 < x \leq 128$ nucleotides), and long ($128 < x \leq 512$ nucleotides). Sequences exceeding 512 nucleotides or containing non-standard nucleotides (non-A, U, C, G) were filtered out, resulting in **7067**, **389**, and **766** sequences for the Pre-training, RL Fine-tuning, and SOLD TEST datasets, respectively. The CASP15 TEST dataset underwent similar filtering for sequences longer than 512 nucleotides and non-AUCG nucleotides, serving as the external test dataset. This process, encompassing clustering, deduplication, and sequence filtering, ensured the dataset’s diversity and consistency, providing a robust foundation for the LDM pre-training, RL fine-tuning, and evaluation.

B. Evaluation Metrics

This section outlines the evaluation metrics used to assess the performance of the SOLD algorithm in RNA design, categorizing them into three groups: one-dimensional metrics for nucleotide-level accuracy, two-dimensional metrics for secondary structure evaluation, and three-dimensional metrics for tertiary structure fidelity.

B.1 One-Dimensional Metrics

The one-dimensional metrics focus on the nucleotide-level accuracy of generated RNA sequences, providing insights into sequence prediction quality. The Sequence Recovery (**Sequence Recovery**) metric quantifies the nucleotide-level prediction accuracy for a single RNA sequence, defined as the proportion of correctly predicted nucleotides:

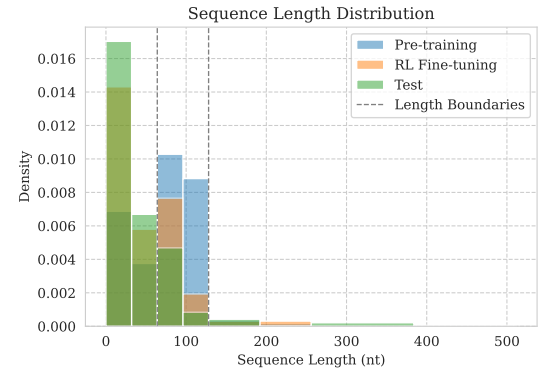


Figure 5: Sequence length distribution across Pre-training, RL Fine-tuning, and SOLD TEST datasets.

$$\text{Sequence Recovery} = \frac{1}{N} \sum_{i=1}^N \mathbf{1} [S_i = \arg \max \mathcal{P}(S_i)] \quad (15)$$

where N is the sequence length, S_i is the ground truth nucleotide at position i , $\mathcal{P}(S_i)$ is the predicted probability distribution over nucleotides (A, U, C, G), and $\mathbf{1}[\cdot]$ is the indicator function (1 if predicted matches ground truth, 0 otherwise). This metric is computed per sequence during validation and averaged across the dataset to assess overall per-sequence accuracy, reflecting the model’s ability to reproduce individual RNA sequences.

The Nucleotide Recovery (**NT Recovery**) metric measures the overall nucleotide-level prediction accuracy across the entire dataset, defined as:

$$\text{NT Recovery} = \frac{\sum_{\text{seq}} \sum_{i=1}^{N_s} \mathbf{1} [S_{s,i} == \arg \max \mathcal{P}(S_{s,i})]}{\sum_{\text{seq}} N_s}, \quad (16)$$

where N_s is the length of sequence s , $S_{s,i}$ is the ground truth nucleotide at position i in sequence s , and $\mathcal{P}(S_{s,i})$ is the predicted probability distribution. This metric aggregates accuracy across all sequences, complementing Sequence Recovery by providing a dataset-wide assessment of nucleotide prediction performance.

B.2 Two-Dimensional Metrics

The two-dimensional metrics evaluate the secondary structure of generated RNA sequences, assessing functional similarity and thermodynamic stability. The Secondary Structure Similarity (**SS**) metric measures the similarity between the predicted secondary structure of the generated sequence and the ground truth, using the ViennaRNA (Lorenz et al. 2011) package to predict structures in dot-bracket notation (dots for unpaired nucleotides, brackets for paired ones). It is calculated as:

$$\text{SS} = \frac{\text{matching}}{\text{length}} \times 100, \quad (17)$$

where matching is the number of positions where predicted and ground truth structures agree (both paired or unpaired),

and length is the sequence length. Expressed as a percentage, SS reflects the functional similarity of the generated sequence’s secondary structure to the target.

The Minimum Free Energy (**MFE**) metric assesses the thermodynamic stability of the generated sequence’s secondary structure, also computed using ViennaRNA. It returns the minimum free energy (in kcal/mol), with lower values indicating greater stability, complementing SS by providing an energetic perspective crucial for RNA functionality.

B.3 Three-Dimensional Metrics

The three-dimensional metrics evaluate the tertiary structure fidelity of generated RNA sequences, comparing predicted 3D structures to ground truth using RhoFold (Shen et al. 2024). The Root Mean Square Deviation (**RMSD**) metric quantifies the average deviation between predicted and ground truth 3D structures, focusing on C4’ backbone atoms. After alignment via the Kabsch algorithm (Kabsch 1976), it is defined as:

$$\text{RMSD} = \sqrt{\frac{1}{N} \sum_{i=1}^N \|\text{true_atom}_i - \text{pred_atom}_i\|^2} + \epsilon, \quad (18)$$

where N is the number of aligned C4’ atoms, true_atom_i and pred_atom_i are the coordinates of the i -th C4’ atom, and $\epsilon = 10^{-6}$ prevents numerical instability. A lower RMSD indicates better structural alignment.

The Local Distance Difference Test (**LDDT**) metric assesses local structural similarity based on C4’ atoms, comparing pairwise distances within a 15.0 Å cutoff. It aggregates the fraction of distances deviating by less than 0.5, 1.0, 2.0, and 4.0 Å (each weighted 0.25), averaged over valid pairs. Scores range from 0 to 1, with higher values indicating better local geometry preservation, complementing RMSD’s global focus.

C. LDM Details

To provide a comprehensive understanding of the Latent Diffusion Model (LDM), this appendix details its network architecture, ablation studies, and comparison with alternative approaches. The LDM generates RNA sequences in a variable-length latent space, leveraging RNA-FM embeddings and backbone geometric features to ensure structural consistency.

C.1 LLM-Related RNA Algorithms

Large Language Models (LLMs) enhance RNA analysis with large RNA sequence datasets (e.g., 36 million for RiNaLMo (Penić et al. 2024)), for example, RNA-FM (Chen et al. 2022) allows structure and function predictions from unannotated data, CodonBERT (Li et al. 2023) optimizes mRNAs, RNA-GPT (Xiao et al. 2024) generates multi-modal alignment sequences, and Nucleotide Transformer (Dalla-Torre et al. 2025) and Evo (Nguyen et al. 2024) extend LLM to DNA/RNA applications. However, the 3D design of the RNA lags behind the AlphaFold2 (Jumper et al. 2021) focused on proteins due to data scarcity.

C.2 Network Architecture

Algorithm 1: LDM Algorithm

```

1: Input: Target distribution  $p(h, c)$  on RNA-FM target
   embedding  $h \in \mathbf{R}^{L \times 640}$  and backbone  $c$ , timestep  $T$ ,
   noise schedule  $\beta_t$ , pre-trained encoder  $\text{Enc}_\psi$ , and de-
   coder  $\text{Dec}_\phi$ 
2: Initialize MLP encoder denoising network  $\pi_\theta$ 
3: while Training do
4:   Sample data with backbone conditioning from the
   dataset:  $(t, h, c) \sim \text{Uniform}(1, \dots, T), p(h, c)$ 
5:   Compressed embeddings:  $z_0 = \text{Enc}_\psi(h)$ 
6:   Generate noisy latent:  $x_t \sim q(x_t | z_0)$ 
7:   Predict target embedding:  $\hat{z}_0 = \pi_\theta(x_t, t, c)$ 
8:   Sample reverse process:  $z_{t-1}$  using Equation 2
9:   Compute loss:  $L = \|z_0 - \hat{z}_0\|^2 - \sum_{i=1}^L \log p_\phi(s_i |$ 
    $\text{Dec}_\phi(\hat{z}_0)_i)$ 
10:  Update parameters:  $\theta \leftarrow \theta - \eta \nabla_\theta L$ 
11: end while
12: return  $\pi_\theta$ 

```

The Latent Diffusion Model (LDM) generates RNA sequences aligned with backbone structures, leveraging RNA-FM embeddings and geometric features.

Figure 1 illustrates the architecture, inspired by RiboDiffusion (Huang et al. 2024a), comprising an MLP encoder, a diffusion network, and an MLP decoder. Unlike RiboDiffusion’s one-hot sequence input ($L, 4$), SOLD utilizes RNA-FM embeddings ($L, 640$), compressed to a latent space ($L, 32$) via a 3-layer MLP encoder. The diffusion network consists of a 4-layer GVP-GNN, incorporating geometric vector perceptrons (Jing et al. 2021) (node hidden dimension 512, edge hidden dimension 128, including dihedral angle features) and a 8-layer Transformer (embedding dimension 512, 16 attention heads, dropout 0.2). The GVP-GNN processes backbone geometric features (e.g., bond angles, bond lengths), while the Transformer captures sequence dependencies, predicting the clean latent embedding. A 3-layer MLP decoder reconstructs the final denoised latent embedding into sequence probabilities ($L, 4$), ensuring length consistency with the input structure. Algorithm 1 presents the LDM training process.

C.3 Ablation Study on Latent Embedding Dimension

Latent Dimension (D)	Sequence Recovery (SOLD TEST)
8	0.5161
16	0.8746
32	0.9768
64	0.9955
128	0.9989

Table 5: Test set recovery rates for different latent dimensions $D \in \{8, 16, 32, 64, 128\}$.

To determine an appropriate latent dimension for subsequent diffusion experiments, we evaluated the impact of compressing RNA-FM embeddings from $(L, 640)$ to (L, D) with $D \in \{8, 16, 32, 64, 128\}$. We measured the best recovery rate on the validation set, defined as the highest recovery rate achieved during training, across different latent dimensions. Figure 6 illustrates the trend of best recovery rates on the validation set as a bar-line chart, showing a general increase with larger dimensions. On the **SOLD TEST** dataset, Table 5 provides detailed recovery rates. The recovery rate improves significantly from $D = 8$ to $D = 64$, but increasing the dimension to $D = 128$ yields only a marginal gain. Considering computational efficiency, $D = 32$ and $D = 64$ strike a strong balance, offering effective latent representations for diffusion-based generation with manageable training times, whereas $D = 8$ and $D = 16$ suffer from notable information loss, and $D = 128$ significantly increases training time for minimal performance improvement.

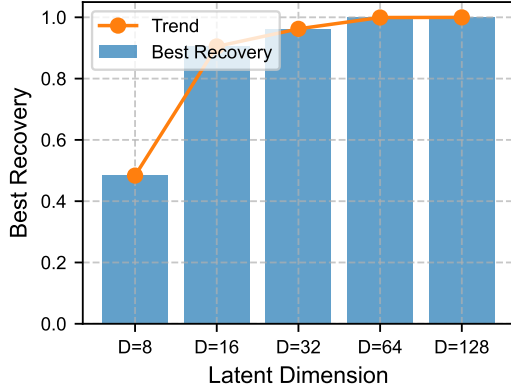


Figure 6: Best recovery rate across different latent dimensions $D \in \{8, 16, 32, 64, 128\}$.

C.4 Optimal Latent Dimension for Generation

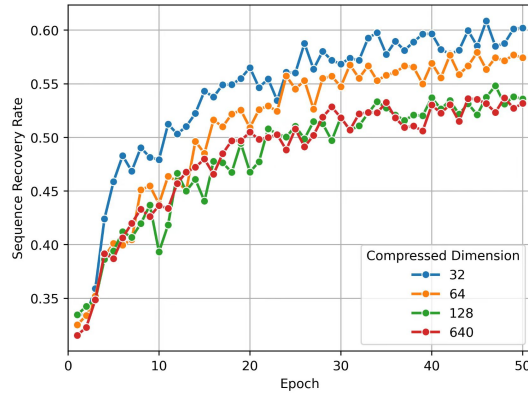


Figure 7: Generative performance of LDM across different latent dimensions D .

To assess the impact of latent dimension D on genera-

tive performance, we extended the ablation study to $D \in \{32, 64, 128, 640\}$, evaluating sequence recovery (Sequence Recovery) on generated RNA sequences. Figure 7 plots the performance trends on the test set, revealing that generative quality peaks at $D = 32$. Increasing D beyond 32 leads to a decline, suggesting that a larger latent space introduces noise and complexity, hindering generation. This mirrors the optimization dilemma noted by Yao et al. (Yao, Yang, and Wang 2025) in image generation, where higher dimensions improve reconstruction but degrade generation due to unconstrained representations. For LDM, $D = 32$ balances generative quality and training efficiency effectively.

C.5 Training Details

The LDM was trained using a standard latent diffusion pipeline, training for 50 epochs with a batch size of 64, utilizing 8 parallel workers and the AdamW optimizer with a learning rate of 0.0001 and weight decay of 0.01. The diffusion process operated over 100 steps. Early stopping was applied with a patience of 10 epochs, monitoring validation recovery with a minimum boost of 0.005. The LDM employed a cosine beta schedule to control noise addition, while sampling procedure supported DDPM and DDIM methods, with DDIM using an eta of 1.0 for stochasticity.

D. SOLD Details

This section provides a theoretical foundation for the SOLD algorithm by deriving an approximate variational objective for its reward maximization, focusing on long-term rewards at $t = 0$ and incorporating instantaneous short-term rewards at $t - 1$ via a piecewise reward switching mechanism. We integrate the DDIM (Song, Meng, and Ermon 2020) framework’s one-step sampling for long-term rewards and the DDPM (Ho, Jain, and Abbeel 2020) framework’s one-step sampling for short-term rewards to construct this objective, validated by ablation studies on SOLD TEST dataset demonstrating improved metrics and faster convergence.

D.1 Approximate Variational Objective for Reward Optimization

This part derives an approximate variational objective for the SOLD algorithm’s reward maximization, ensuring practical convergence for its fine-tuning phase. We leverage the DDIM framework’s one-step sampling from z_t to z'_0 for long-term rewards and the DDPM framework’s one-step sampling from z_t to z'_{t-1} for short-term rewards, both designed for efficiency rather than the full multi-step ELBO used in methods like DDPO (Black et al. 2023) and DPOK (Fan et al. 2023). Rewards are integrated using a piecewise function, prioritizing short-term rewards in early denoising steps and long-term rewards in later steps.

The SOLD objective is defined as:

$$\mathcal{J}_{\text{SOLD}}(\theta) = \mathbf{E}_{t \sim \mathcal{U}[1, T], c, z_t, z'_{t-1}, z'_0 \sim p_{\theta}(z'_{t-1}, z'_0 | z_t, c)} [r_{\text{total}}(t)], \quad (19)$$

where:

- t is a uniformly sampled timestep,
- c is the conditioning input (RNA structure),

- z_t is the noised sequence,
- $z'_{t-1} \sim p_\theta(z'_{t-1} \mid x_t, c)$ is the optimized intermediate sequence.
- $z'_0 \sim p_\theta(x'_0 \mid z_t, c)$ is the final decoded sequence.
- $r_{\text{total}}(t)$ is a piecewise reward function, defined as:

$$r_{\text{total}}(t) = \begin{cases} R_i(z'_{t-1}) & t \geq \tau, \\ R_i(z'_0) & t < \tau, \end{cases} \quad (20)$$

where τ is a tunable threshold parameter that determines the switching point between short-term and long-term rewards, R_i represents the reward function for objective $i \in \{\text{MFE, SS, LDDT}\}$, and both z'_{t-1} and z'_0 are derived from the network's predictions conditioned on z_t and c . Specifically, $R_i(z'_{t-1})$ denotes the short-term reward, evaluated on the intermediate sequence z'_{t-1} and typically utilized in the early denoising steps to guide the process toward feasible intermediate states, while $R_i(z'_0)$ represents the long-term reward, assessed on the final decoded sequence z'_0 and employed in the later denoising steps to optimize the overall stability and quality of the generated sequence.

The forward diffusion process follows:

$$q(z_t \mid z_{t-1}) = \mathcal{N}(z_t; \sqrt{1 - \beta_t} z_{t-1}, \beta_t I), \quad (21)$$

with the cumulative noised sequence:

$$z_t = \sqrt{\bar{\alpha}_t} z_0 + \sqrt{1 - \bar{\alpha}_t} \epsilon, \quad \epsilon \sim \mathcal{N}(0, I), \quad (22)$$

where $\bar{\alpha}_t = \prod_{s=1}^t (1 - \beta_s)$ aggregates the variance schedule β_t .

The reverse sampling processes are approximated as:

- short-term (from t to $t-1$): $z'_{t-1} = \sqrt{\bar{\alpha}_{t-1}} \hat{z}_\theta(z_t, t) + \sqrt{\beta_t} \epsilon$,
- long-term (from t to 0): $z'_0 = \sqrt{\bar{\alpha}_0} \hat{z}_\theta(z_t, t) + \sigma_{t,0} \epsilon$,

where $\bar{\alpha}_0 = 1$, $\hat{z}_\theta(z_t, t)$ is the network's prediction of the clean sequence, β_t is the noise schedule, and $\sigma_{t,0}$ is derived from the variance schedule.

The reverse distributions are modeled as:

$$\begin{aligned} p_\theta(z'_{t-1} \mid z_t) &= \mathcal{N}(\hat{z}_\theta(z_t, t), \beta_t I), \\ p_\theta(z'_0 \mid z_t) &= \mathcal{N}(\hat{z}_\theta(z_t, t), \sigma_{t,0}^2 I), \end{aligned} \quad (23)$$

where β_t and $\sigma_{t,0}^2$ reflect the respective noise levels.

The approximate variational objective is based on the reward-weighted log-likelihood:

$$J_{\text{SOLD}} = \mathbf{E}_{t,c,z_t,z'_{t-1},z'_0} [r_{\text{total}}(t) \log p_\theta(z'_s)], \quad (24)$$

where z'_s is z'_{t-1} for $t \geq \tau$ and z'_0 for $t < \tau$.

The gradient of the objective is:

$$\nabla_\theta J_{\text{SOLD}} \propto \mathbf{E}_{t,c,z_t,z'_{t-1},z'_0} [r_{\text{total}}(t) \nabla_\theta \log p_\theta(z'_s \mid z_t)]. \quad (25)$$

Under the condition where $\tau = T$ (focusing solely on long-term rewards), $r_{\text{total}}(t) = R_i(z'_0)$ for all t , reducing the SOLD objective to:

$$\nabla_\theta J_{\text{SOLD}} \approx \mathbf{E}_{t,c,z_t,z'_0} [R_i(z'_0) \nabla_\theta \log p_\theta(z'_0 \mid z_t)]. \quad (26)$$

The evidence lower bound (ELBO) for $\log p_\theta(z'_0)$ is:

$$\log p_\theta(z'_0) \geq \mathbf{E}_{q(z_{1:T} \mid z_0)} \left[\log \frac{p_\theta(z'_{0:T} \mid c)}{q(z_{1:T} \mid z_0)} \right]. \quad (27)$$

Given DDIM's one-step sampling efficiency, we use a single-step approximation:

$$\log p_\theta(z'_0) \geq \mathbf{E}_{q(z_t \mid z_0)} \left[\log \frac{p_\theta(z'_0 \mid z_t, c) p(z_t)}{q(z_t \mid z_0)} \right]. \quad (28)$$

Simplifying, we obtain:

$$\log p_\theta(z'_0) \geq \mathbf{E}_{q(z_t \mid z_0)} [\log p_\theta(z'_0 \mid z_t, c)] + C, \quad (29)$$

where C is a θ -independent constant:

$$C = \mathbf{E}_{q(z_t \mid z_0)} [\log p(z_t)] - \mathbf{E}_{q(z_t \mid z_0)} [\log q(z_t \mid z_0)]. \quad (30)$$

The gradient of the DDPO objective, based on the DDPM full-step sampling to obtain z_0^{full} , is:

$$\nabla_\theta J_{\text{DDPO}} \propto \mathbf{E}_{q(z_t \mid z_0)} [R_i(z_0^{\text{full}}) \nabla_\theta \log p_\theta(z_0^{\text{full}} \mid z_t)]. \quad (31)$$

For SOLD, the long-term reward is derived from the DDIM one-step sampling, yielding z'_0 . Under the assumption that the DDPM full-step sampling converges to a distribution close to the DDIM one-step sampling for z'_0 , with bounded prediction error, we approximate $z_0^{\text{full}} \approx z'_0$. Under this approximation, we obtain:

$$\nabla_\theta J_{\text{DDPO}} \approx \nabla_\theta J_{\text{SOLD}}(\theta). \quad (32)$$

This demonstrates that, in the extreme case where $\tau = T$ and DDPM's full-step sampling closely approximates DDIM's one-step sampling for the final sequence z'_0 , SOLD's optimization reduces to an equivalent form of DDPO's objective, leveraging the efficiency of a single-step process to reduce complexity per iteration. Moreover, experimental results reveal that integrating short-term rewards with long-term rewards through the tunable threshold τ yields superior performance. Algorithm 2 illustrates the single-step optimization process in SOLD.

D.2 Piecewise Reward Strategy Abalation

To enhance the optimization of the SOLD algorithm, we introduce a piecewise reward strategy that integrates instantaneous rewards r_t (via DDPM one-step sampling) and long-term rewards r_0 (based on the final decoded sequence x'_0 via DDIM one-step sampling). This approach utilizes the dense feedback of r_t in early denoising steps for effective initial guidance and the stability of r_0 in later steps for final optimization, with the transition controlled by a tunable threshold τ .

We conducted an ablation study to evaluate the performance of different reward configurations across three objectives: MFE, SS, and LDDT. Each objective was tested with five settings: long-term reward only, short-term reward only, and mixed reward strategies with $\tau = 90$, $\tau = 60$, and $\tau = 20$, where the total diffusion steps are 100. The mixed reward strategy prioritizes short-term rewards for $t \geq \tau$ and transitions to long-term rewards for $t < \tau$.

Algorithm 2: SOLD Algorithm

- 1: **Input:** Target distribution $p(h, c)$ on compressed target embedding $z \in \mathbf{R}^{L \times D}$ and backbone c , pre-trained model π_θ , timestep T , reward function R_i , weighting functions $w(t)$ and $u(t)$, learning rate η , KL weights λ_{ref}
- 2: Initialize $\theta_{\text{old}} \leftarrow \theta$
- 3: **while** θ not converged **do**
- 4: Sample data with backbone conditioning from the dataset: $(t, z_0, c) \sim \text{Uniform}(1, \dots, T), p(z, c)$
- 5: Calculate noisy latent $z_t \sim q(z_t | z_0)$
- 6: Predict target embedding $\hat{z}_0 = \pi_\theta(z_t, t, c)$
- 7: Calculate optimized embedding z'_0 using Equation (7), decode s'_0 from z'_0 to calculate long-term reward
- 8: Calculate z_{t-1} from \hat{z}_0 as the reverse process defined in Equation (2), then decode z_{t-1} into s_{t-1} to calculate short-term reward
- 9: Calculate reward $r_{\text{total}}(t)$ using Equation (8), and then normalized rewards across batch samples to reduce high variance.
- 10: Calculate importance weight $w = \frac{p_\theta(z'_0 | z_t, c, t)}{p_{\text{ref}}(z'_0 | z_t, c, t)}$
- 11: Calculate gradient:

$$g = w \cdot \nabla_\theta \log p_\theta(z'_0 | z_t, c, t) \cdot r_{\text{total}}(t)$$
- 12: Calculate KL penalties:

$$\text{KL}_{\text{ref}} = D_{\text{KL}}(p_\theta | p_{\text{ref}})$$
- 13: Update parameters:

$$\theta \leftarrow \theta + \eta (g - \lambda_{\text{ref}} \nabla_\theta \text{KL}_{\text{ref}})$$
- 14: Update old policy: $\theta_{\text{old}} \leftarrow \theta$
- 15: **end while**
- 16: **return:** π_θ

Table 6 summarizes the experimental results for each setting on the SOLD TEST dataset, revealing notable trends across the objectives. For MFE and LDDT, the mixed strategy with a higher τ value tends to outperform single-reward settings, suggesting that a later transition to long-term rewards enhances stability. For SS, an intermediate τ value appears to strike the best balance between short-term guidance and long-term optimization, indicating a more effective integration of both reward types. These observations suggest that the mixed reward approach adapts effectively to each objective, with the optimal τ varying based on the specific requirements of stability, structure, and accuracy.

Figure 8 illustrates the reward trends for MFE, SS, and LDDT over epochs. These visualizations highlight the complementary dynamics of the mixed reward approach, bridging the early exploration of short-term rewards and the later exploitation of long-term rewards, with hyperparameters tuned as follows: for MFE and LDDT, long-term reward dominates the last 90 steps and short-term the first 10 steps; for SS, long-term dominates the last 60 steps and short-term the first 40 steps.

D.3 Training Details

For training the SOLD algorithm, we implemented an online reinforcement learning (RL) training pipeline using the Proximal Policy Optimization (PPO) algorithm, incorporating techniques inspired by DPOK to ensure stability and ef-

Setting	SOLD TEST
MFE Training (MFE reward) ↓	
Long-term only	-17.2421
Short-term only	-17.7265
$\tau = 90$	-19.7428
$\tau = 60$	-18.7498
$\tau = 20$	-17.4660
SS Training (SS reward) ↑	
Long-term only	0.7494
Short-term only	0.7522
$\tau = 90$	0.7496
$\tau = 60$	0.7551
$\tau = 20$	0.7548
LDDT Training (LDDT reward) ↑	
Long-term only	0.6326
Short-term only	0.6313
$\tau = 90$	0.6384
$\tau = 60$	0.6371
$\tau = 20$	0.6338

Table 6: Ablation study results for piecewise reward strategies across MFE, SS, and LDDT objectives with $\tau = 90$, $\tau = 60$, and $\tau = 20$ on the SOLD TEST dataset.

iciency. The training process spanned 100 epochs, with a batch size of 32 sequences, leveraging 8 parallel workers for data loading. Time steps t were sampled uniformly from $[1, T]$, where $T = 100$, as specified in the configuration.

The reward computation followed a piecewise reward strategy, utilizing a threshold-based approach where short-term rewards dominate for $t > \tau$ and long-term rewards for $t \leq \tau$. Reward components were computed as a weighted combination of multiple objectives: $r = w_{\text{SS}} \cdot \text{SS} + w_{\text{MFE}} \cdot \text{MFE} + w_{\text{LDDT}} \cdot \text{LDDT}$, with weights $w_{\text{SS}} = 0.0$, $w_{\text{MFE}} = 1.0$, and $w_{\text{LDDT}} = 0.0$ for the specific run, adjusted based on the objective (e.g., MFE focused in the provided configuration). Rewards were calculated using 16 parallel jobs for efficiency.

The PPO optimization employed a clipped surrogate loss with a clip range of 0.0001. Advantages were estimated as $A = \frac{r - \mu_r}{\sigma_r + 10^{-8}}$, where r is the reward, and μ_r and σ_r are the mean and standard deviation of the rewards within a batch, ensuring normalized advantage estimates. Gradients were accumulated over 32 steps before each parameter update, using the AdamW optimizer with a learning rate of 10^{-5} and a weight decay of 0.001. Gradient clipping was applied with a maximum norm of 1.0 to prevent exploding gradients. Batch normalization weights were frozen to align with the pre-trained model, enhancing stability.

KL regularization was implemented to prevent overfitting and preserve the pre-trained model's capabilities. The KL divergence between the current model p_θ and the reference model p_{ref} was computed as $\text{KL} = 0.5 \cdot \mathbb{E}[(\log p_\theta - \log p_{\text{ref}})^2]$, weighted by $\alpha = 1.0$, to encourage exploration while maintaining stability. The total loss was formulated as

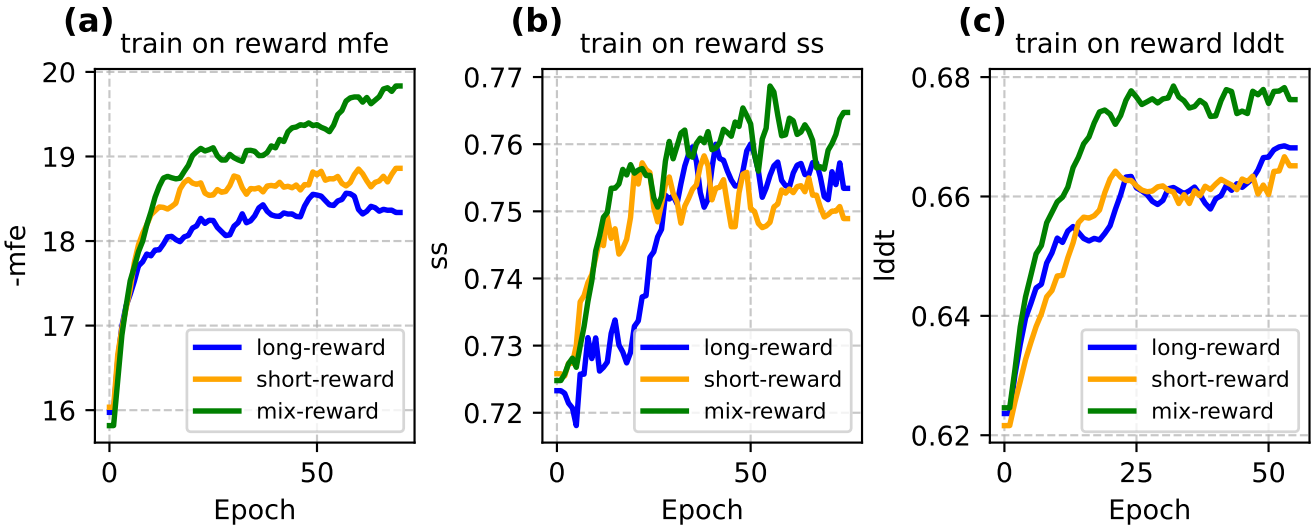


Figure 8: Validation results for **long-term reward**, **short-term reward**, and **mixed reward** settings with MFE, SS, and LDDT as reward objectives: (a) MFE, (b) SS, (c) LDDT.

$L = L_{\text{policy}} + \alpha \cdot \text{KL}_{\text{ref}}$, balancing policy optimization with regularization.

E. Other RNA Inverse Folding algorithms

This appendix provides detailed implementations and reproduction protocols for state-of-the-art RNA inverse-folding algorithms compared in this study, ensuring fair and reproducible performance evaluation. We include comprehensive descriptions of training pipelines, architectural configurations, datasets, and evaluation metrics for each method, facilitating transparency and validation.

E.1 RhoDesign Algorithm Reproduction Details

To ensure a fair comparison with SOLD, we reproduced the RhoDesign (Wong et al. 2024) algorithm, originally provided with inference code only (<https://github.com/ml4bio/RhoDesign>), based on its described variational autoencoder (VAE) framework. Unlike the original implementation, which leveraged RhoFold to predict 3D structures for 369,499 RNACentral sequences to augment training data, we adhered to a controlled experimental setup. Specifically, we utilized the pre-training dataset detailed in Appendix B as the training set, without incorporating additional predicted structures, to maintain consistency and fairness across all methods evaluated.

Training was implemented in PyTorch, processing PDB files from the pre-training dataset to extract structural coordinates. We employed the Biotite library to ensure consistent atom counts, focusing on key atoms relevant to RNA backbone representation, though specific atom selections (e.g., C4', C1', N1) were aligned with default settings to match the original methodology. The model was trained for 100 epochs with batch size of 32, learning rate of 10^{-5} , and the Adam optimizer on an NVIDIA A100 GPU. Evaluation was conducted on the SOLD TEST dataset and the CASP15 TEST

dataset, using the sequence recovery rate as the primary metric, with early stopping applied after 10 epochs without improvement (minimum boost threshold of 0.005 on Sequence Recovery).

E.2 RDesign Algorithm Reproduction Details

To reproduce the RDesign (Tan et al. 2024) algorithm, we utilized its public available source code (<https://github.com/A4Bio/RDesign>). The model architecture was maintained consistent with the original implementation, featuring a 3-layer MPNN encoder and decoder. Training was conducted on an NVIDIA A100 GPU, using the Adam optimizer with a learning rate of 0.0003, batch size of 32, and 100 epochs. Mixed precision training with GradScaler (initial scale 4096) and a 0.1 dropout rate were applied, also with early stopping after 10 epochs no boost.

E.3 gRNADe Algorithm Reproduction Details

To reproduce the gRNADe (Joshi et al. 2025) algorithm, we utilized its open-source code (<https://github.com/chaitjo/geometric-rna-design>). The training pipeline was implemented with PyTorch Geometric, processing the SOLD pre-training dataset, where each PDB ID corresponds to a single conformation, unlike the original gRNADe setting that leverages multiple conformations per PDB ID to address structural dynamics. The RNAGraphFeaturizer module constructed a 32-nearest-neighbor graph using a 3-bead coarse-grained representation (P, C4', N1/N9). The model replicated a 4-layer multi-state GVP-GNN encoder (node dimensions (128,16), edge dimensions (64,4), dropout 0.5) and a 4-layer autoregressive GVP-GNN decoder with SE(3)-equivariant updates and Deep Set pooling, trained with cross-entropy loss (label smoothing 0.05). Training ran on an NVIDIA A100 GPU for 100 epochs, using the Adam optimizer with a learning

Method	Sequence Recovery \uparrow	MFE \downarrow	SS \uparrow	RMSD \downarrow	LDDT \uparrow
SOLD TEST (short)					
RhoDesign	0.2655 \pm 0.0492	-4.4230 \pm 1.664	0.7043 \pm 0.0788	12.2489 \pm 3.5662	0.5513 \pm 0.0542
RDesign	0.4691 \pm 0.0720	-3.6376 \pm 1.5571	0.6636 \pm 0.1293	11.8251 \pm 4.4616	0.5787 \pm 0.0877
gRNADe	0.5187 \pm 0.0837	-2.9642 \pm 1.5130	0.6034 \pm 0.1184	13.7774 \pm 4.6913	0.5309 \pm 0.0751
RiboDiffusion	0.5459 \pm 0.0600	-6.1953 \pm 1.3701	0.8203 \pm 0.0831	8.1286 \pm 2.1961	0.6642 \pm 0.0535
DRAKES	0.4529 \pm 0.0563	-6.9797 \pm 1.2297	0.8369 \pm 0.0434	7.9829 \pm 1.9218	0.6716 \pm 0.0572
LDM	0.6035 \pm 0.0354	-5.6705 \pm 1.3069	0.7906 \pm 0.0747	7.9229 \pm 1.7964	0.6848 \pm 0.0443
SOLD	0.5915 \pm 0.0468	-7.0453 \pm 1.3316	0.8251 \pm 0.0769	7.6320 \pm 2.1259	0.6984 \pm 0.0508
SOLD TEST (medium)					
RhoDesign	0.2984 \pm 0.0291	-20.1741 \pm 3.7921	0.4919 \pm 0.1017	23.9709 \pm 3.6882	0.3552 \pm 0.0436
RDesign	0.3745 \pm 0.0366	-17.2209 \pm 3.8661	0.4637 \pm 0.1009	24.5116 \pm 3.7689	0.3545 \pm 0.0484
gRNADe	0.4908 \pm 0.0414	-18.2801 \pm 4.2355	0.4405 \pm 0.0870	26.0511 \pm 3.8313	0.3410 \pm 0.0445
RiboDiffusion	0.4048 \pm 0.0446	-26.8418 \pm 4.2664	0.6409 \pm 0.0865	20.2351 \pm 3.5920	0.4636 \pm 0.0616
DRAKES	0.4036 \pm 0.0335	-23.6893 \pm 3.8733	0.6634 \pm 0.0620	19.2688 \pm 3.0542	0.4751 \pm 0.0491
LDM	0.4754 \pm 0.0271	-22.2533 \pm 3.2741	0.5405 \pm 0.0941	22.5351 \pm 3.0984	0.4018 \pm 0.0555
SOLD	0.5193 \pm 0.0247	-28.4233 \pm 3.0945	0.6676 \pm 0.0488	19.0019 \pm 3.1009	0.4835 \pm 0.0557
SOLD TEST (long)					
RhoDesign	0.3008 \pm 0.0219	-85.9170 \pm 7.8836	0.4186 \pm 0.0569	47.2802 \pm 4.6981	0.3228 \pm 0.0172
RDesign	0.3558 \pm 0.0205	-84.2757 \pm 7.1098	0.4139 \pm 0.0541	47.2937 \pm 4.0661	0.3197 \pm 0.0185
gRNADe	0.4686 \pm 0.0222	-87.1803 \pm 8.5181	0.3974 \pm 0.0471	49.0031 \pm 4.9398	0.3191 \pm 0.0200
RiboDiffusion	0.4034 \pm 0.0268	-98.8963 \pm 8.0511	0.5591 \pm 0.0550	43.3506 \pm 3.5654	0.3488 \pm 0.0228
DRAKES	0.3817 \pm 0.0186	-81.3017 \pm 6.4232	0.5437 \pm 0.0475	43.0538 \pm 2.2279	0.3490 \pm 0.0202
LDM	0.4672 \pm 0.0169	-87.3374 \pm 6.4215	0.4595 \pm 0.0572	47.3536 \pm 4.5370	0.3303 \pm 0.0219
SOLD	0.4962 \pm 0.0138	-111.3642 \pm 5.4817	0.5633 \pm 0.0488	42.6735 \pm 3.0404	0.3524 \pm 0.0220

Table 7: Multi-Objective Performance Comparison across Different RNA Sequence Length

rate of 0.0001, a maximum of 3000 nodes per batch, with a DataLoader using 4 workers and BatchSampler.

Evaluation also utilized the SOLD TEST dataset and CASP15 TEST dataset, focusing on recovery rate, with early stopping after 10 epochs (minimum boost 0.005 on recovery as previous algorithms). The reproduced performance validated gRNADe’s design capabilities, adapted to our single-conformation context, serving as a benchmark for SOLD’s enhancements.

E.4 RiboDiffusion Algorithm Reproduction Details

To reproduce the RiboDiffusion (Huang et al. 2024a) algorithm, for tertiary structure-based RNA inverse folding, we utilized the described methodology and available code (<https://github.com/ml4bio/RiboDiffusion>), noting that RiboDiffusion did not provide training code, with implementation details inferred from the original paper. The training pipeline utilized the SOLD pretraining dataset. The model replicated a dual-module design: a 4-layer GVP-GNN structure module (node dimensions (512,128), edge dimensions (128,1), dropout 0.1) and an 8-layer Transformer sequence module (512-dimensional embedding, 16 attention heads), trained with a variational diffusion SDE (cosine schedule, beta 0.1 to 20) using weighted mean squared error loss. Training ran on an NVIDIA A100 GPU for 1000 epochs, using the AdamW optimizer (learning rate 0.0001, batch size 1, gradient clipping 100), 8-step gradient accumulation,

0.999 EMA decay for stability, and a DataLoader with 0.1 Å Gaussian noise.

E.5 DRAKES Algorithm Reproduction Details

To reproduce the DRAKES (Wang et al. 2024) algorithm, proposed for fine-tuning discrete diffusion models to optimize reward functions, we utilized the open-source code (<https://github.com/ChenyuWang-Monica/DRAKES>) and described methodology. The training pipeline, a two-stage process, used the SOLD pre-training dataset. In the first stage, we trained a masked discrete diffusion model, extracting RNA 3D structure coordinates and sequences, with preprocessing including 10-nearest-neighbor geometric features (16 RBF and 16 positional encodings) and 0.1 Å Gaussian noise. The model architecture replicated a 3-layer MPNN encoder and 3-layer decoder (node features 128, edge features 128, hidden dimension 128, dropout 0.1), outputting 5 base probabilities, initialized with Xavier uniform distribution.

Training for the first stage ran for 100 epochs, using the AdamW optimizer (learning rate 0.0001, weight decay 0.0001, batch size 4) with 4 workers. In the second stage, we first pre-trained a reward model on the SOLD dataset to predict RNA stability (MFE via RNAfold), using mean pooling over the last layer of the first-stage model followed by an MLP, trained for 100 epochs with the AdamW optimizer (learning rate 0.0001, weight decay 0.0001, batch

size 4, early stopping patience 10). The diffusion model was then fine-tuned during the DRAKES optimization phase using the pre-trained diffusion checkpoint and reward checkpoint, with a masked interpolant diffusion (200 timesteps). Fine-tuning ran for 50 epochs with the AdamW optimizer (learning rate 0.0001, weight decay 0.0001, batch size 8), early stopping (patience 10), KL divergence regularization with a proportion of 0.1, and Gumbel-Softmax with a linear temperature schedule.

F. Exploration of Length Effects and Computational Efficiency

This section presents a comprehensive evaluation of SOLD for RNA inverse folding, focusing on its multi-objective performance, stability, and computational efficiency across varying sequence lengths. We analyze SOLD and its base LDM against SOTA RNA inverse folding methods, including RhoDesign, RDesign, gRNAd, RiboDiffusion, and DRAKES, on the SOLD TEST Dataset. Test dataset is partitioned into short (≤ 64 nucleotides), medium ($64 < x \leq 128$ nucleotides), and long ($128 < x \leq 512$ nucleotides) sequences as described in appendix A. Additionally, we evaluate SOLD’s computational efficiency by measuring sampling time and GPU memory usage for generating sequences across diverse RNA structures.

F.1 Multi-Objective Performance Analysis of Sequence Length

We evaluated SOLD across different sequence length to assess its robustness in designing RNA structures of varying complexity. As shown in Table 7, LDM achieves the highest Sequence Recovery across short, medium, and long sequence ranges, outperforming baseline methods such as RiboDiffusion and gRNAd. SOLD, enhanced through RL fine-tuning, further improves all metrics, achieving optimal or near-optimal results across all length categories. Notably, in the long sequence range, SOLD significantly surpasses RDesign and gRNAd in MFE, SS, and LDDT, demonstrating its ability to generate sequences with high structural fidelity and biological functionality.

Among baselines, gRNAd and RDesign perform well on short sequences but exhibit declining performance in medium and long ranges. RiboDiffusion and DRAKES show competitive performance in short and medium sequences but fall short of SOLD in long sequences. In terms of stability, SOLD exhibits the almost lowest standard deviations across all metrics, surpassing LDM and other baselines, indicating high prediction consistency suitable for precision RNA design.

As sequence length increases, Sequence Recovery, SS, and LDDT tend to decrease, MFE becomes more negative, and RMSD increases, reflecting the challenges of complex RNA folding. SOLD effectively mitigates these challenges, maintaining robust performance and stability.

F.2 Computational Efficiency

To evaluate the computational efficiency of SOLD, we measured the sampling time and GPU memory usage required

to generate eight RNA sequences for PDB structures with varying sequence lengths. As shown in Table 8, sampling time increases moderately with sequence length, remaining within seconds from short (77 nucleotides) to long (501 nucleotides) sequences. GPU memory usage rises slightly but stays manageable across all lengths.

PDB ID	Length	Time (s)	Memory (MB)
2CKY_1_A	77	37.04	7734
7PKT_1_1	162	42.08	7974
7PUA_1_CA	501	50.99	8433

Table 8: Sampling time and GPU memory usage for generating eight sequences per PDB structure.

F.3 Significance Testing on SOLD TEST Dataset

To evaluate differences among all methods used for the RNA inverse folding problem, we conducted significance testing across sequence and structure metrics. Due to non-normal distributions (confirmed by Shapiro-Wilk tests, $p < 0.05$), we employed non-parametric tests.

The **Friedman test** was used to assess overall differences across the seven methods for each metric, suitable for paired samples across multiple groups. When significant differences were detected ($p < 0.05$), we performed **pairwise Wilcoxon signed-rank tests** to compare method pairs (21 comparisons). To account for multiple comparisons, we applied Bonferroni correction ($\alpha = 0.05/21 \approx 0.00238$). Effect sizes were computed as $r = Z/\sqrt{N}$, where Z is the Wilcoxon statistic and N is the number of pairs. Results in Figure 9 are visualized using boxplots for metric distributions and p-value heatmaps for pairwise significance.

The analysis revealed significant differences among methods, with SOLD demonstrating significant superiority over all other methods across all metrics, except for RMSD, where SOLD’s performance was comparable to DRAKES.

G. Additional Design Cases

To comprehensively evaluate the performance and robustness of SOLD, this appendix presents additional inverse folding case studies on four distinct RNA targets sourced from the Protein Data Bank (PDB IDs: 5MOJ, 4NYB, 8SFQ, and 7SZU), as shown in Figure 10 and Figure 11. These targets feature diverse sequence lengths (ranging from 28 to 79 nucleotides) and structural complexities.

For each target, we provide a head-to-head performance comparison of SOLD against six baseline methods: LDM, DRAKES, RiboDiffusion, gRNAd, RDesign and RhoDesign. Because SOLD’s predictions are exceptionally accurate, in the visualizations we superimpose its predicted structure (blue) directly onto the ground-truth structure (gold) to highlight this high fidelity. In contrast, the structures generated by baseline methods exhibit significant deviations. This striking difference underscores SOLD’s superior accuracy and its reliability in solving the RNA inverse folding problem across a variety of structural challenges.

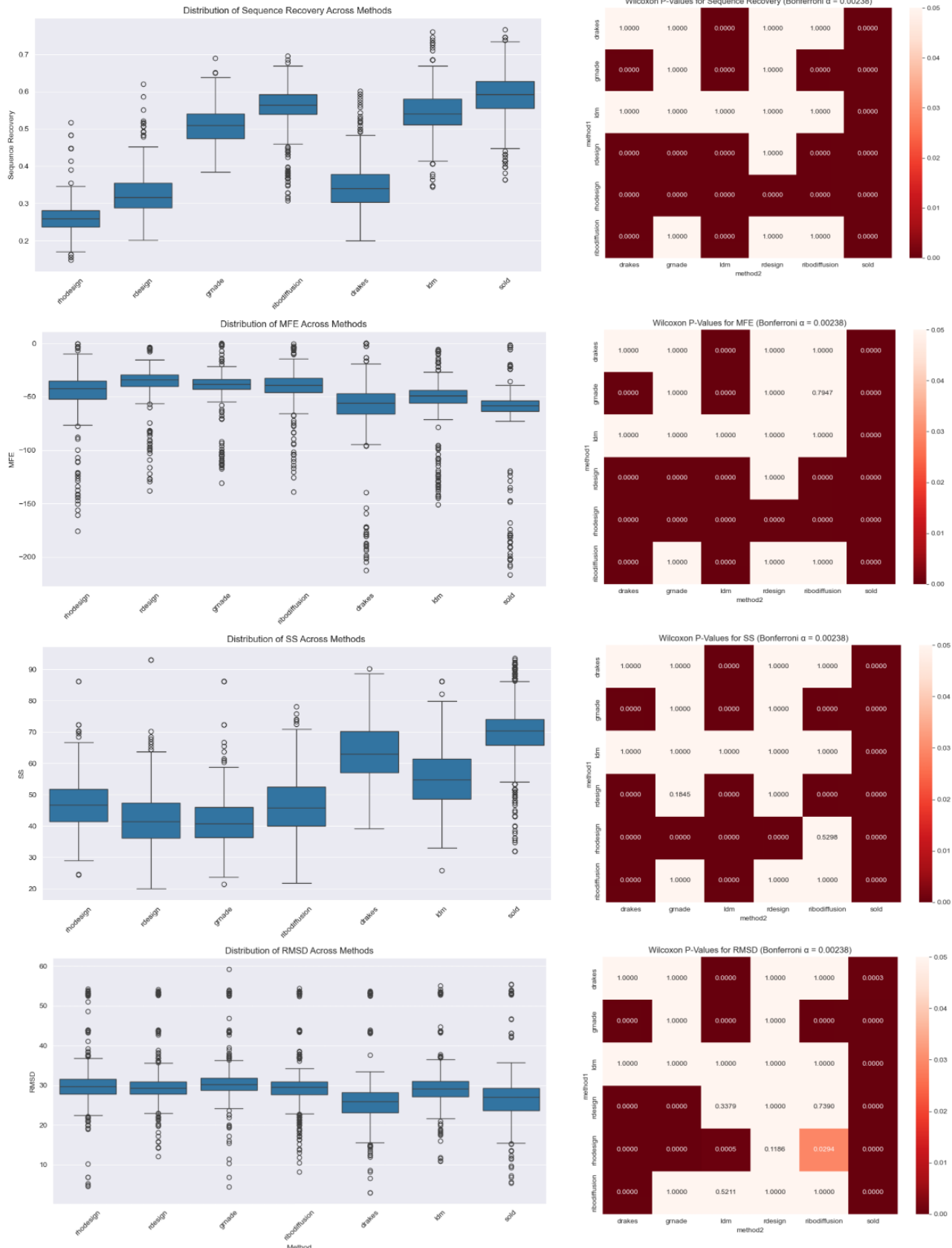


Figure 9: Significant for Sequence and Structure Metrics on SOLD TEST dataset

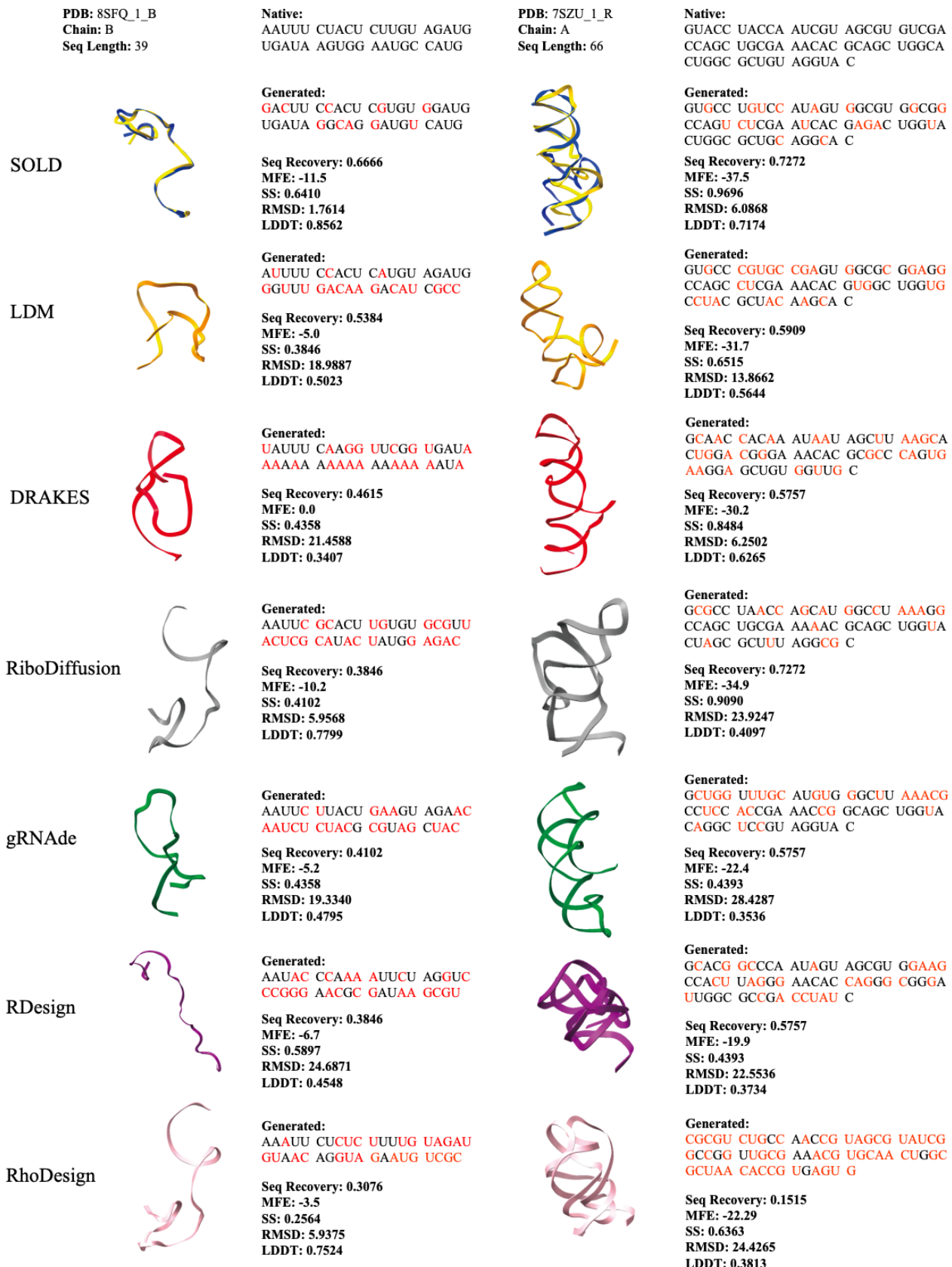


Figure 10: Additional Successful RNA Designs using the SOLD Model (Part I)

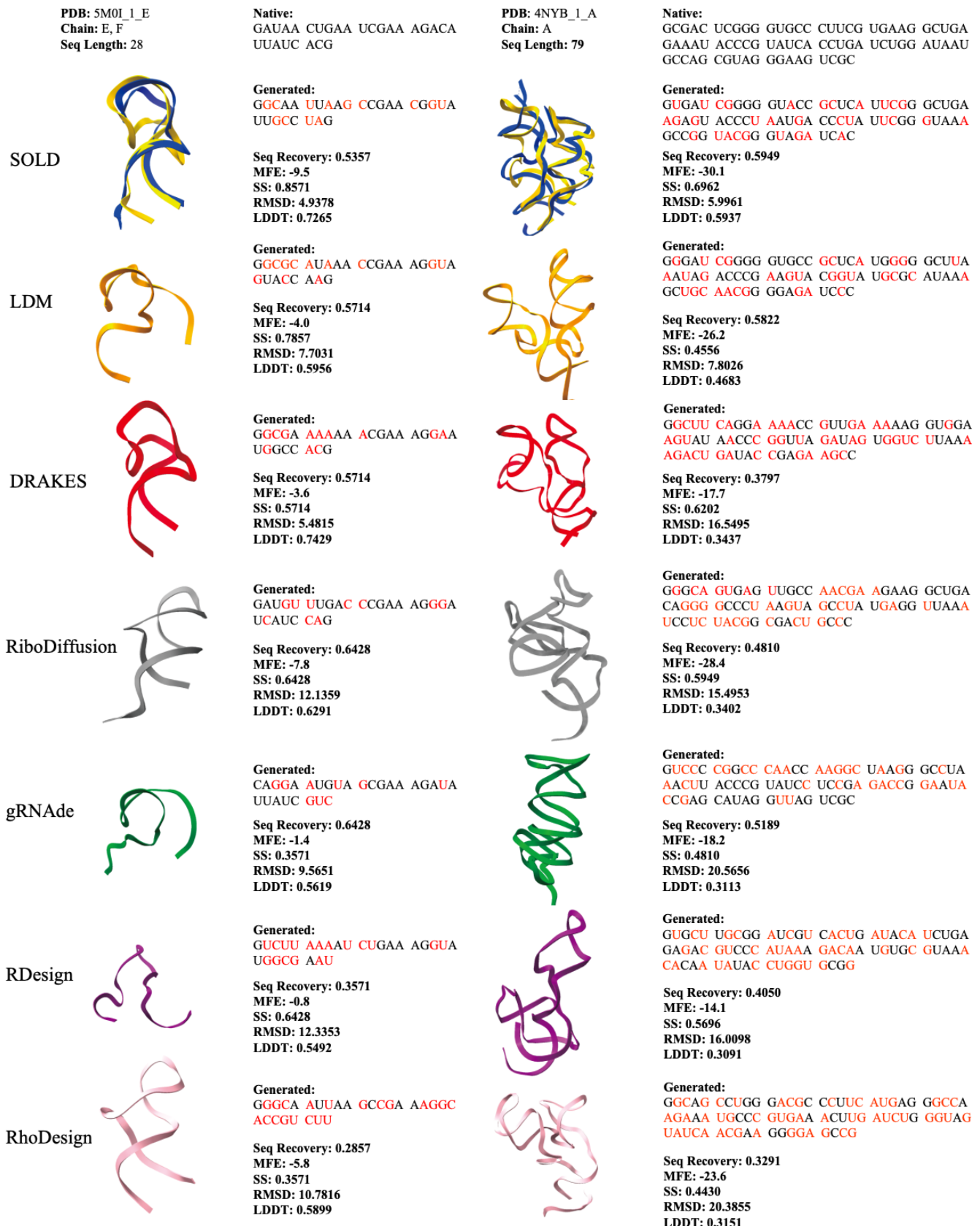


Figure 11: Additional Successful RNA Designs using the SOLD Model (Part II)